Demonstration system of pumped heat energy storage (PHES) and its round-trip efficiency

Muhammad Tahir Ameen [a,b], Zhiwei Ma [c,*], Andrew Smallbone [c], Rose Norman [a], Anthony Paul Roskilly [c]

[a] School of Engineering, Newcastle University, Newcastle upon Tyne NE1 7RU, United Kingdom
[b] Department of Mechanical Engineering, University of Engineering and Technology, Lahore 54890, Pakistan
[c] Department of Engineering, Durham University, Durham DH1 3LE, United Kingdom

HIGHLIGHTS

- World's first grid-scale PHES demonstrator system has been described.
- Performance of a novel heat pump/engine has been tested and losses are quantified.
- Round-trip efficiency of the system has been identified numerically.
- Round-trip efficiency is within a range of 70–80 % for single storage cycle.
- Periodic operation can yield a steady global round-trip efficiency of about 73 %.

ARTICLE INFO

ABSTRACT

Among the known energy storage technologies aiming to increase the efficiency and stability of power grids, Pumped Heat Energy Storage (PHES) is considered by many as a promising candidate because of its flexibility, potential for scale-up and low cost per energy storage unit. Whilst there are numerous demonstration systems under development, as it stands the only PHES demonstration system to be realised at scale is located in Hampshire, UK. This paper aims to present the results and analysis obtained from its commissioning and testing as part of an on-going study. The system was designed to offer a nominal power size of 150 kW$_e$ and energy storage capacity of 600 kWh$_e$ for an 8-hour storage cycle. This work presents evidence of the system Round-trip efficiency (RTE), which is considered as a fundamental performance metric for large-scale energy storage technologies. Recorded Pressure-Volume (P-V) measurements from recent heat pump/engine testing at part-load offers useful insight in terms of overall performance. Models are also developed to simulate the system to finally predict the performance at full-load conditions. The system and principle of operation are described first, followed by mathematical modelling outlining heat transfer mechanism and associated key losses involved in thermodynamic processes within components, and finally results are presented and compared at different operating conditions using different working gases. The results show good agreement with earlier studies, which indicate that expected electricity-to-electricity RTE is quite comparable to other mature technologies such as Pumped Hydropower Storage and Compressed Air Energy Storage. The cyclic operation of the system is also discussed. One-off storage cycle results in lower RTEs compared to a load-levelling cyclic operation where the efficiency is significantly improved due to stable packed-bed behaviour and better utilisation after an initial transient state.

1. Introduction

Energy demand is increasing in both domestic and industrial sectors.

At the same time surging carbon emissions and risks because of depletion of fossil fuel reserves have brought a shift in trend in energy management. Renewable energy sources (RES) – such as wind, solar and geothermal energies are widely researched and utilised to reduce the

Nomenclature

A	store area, m^2
A_v	open area of screen valve, m^2
A_w	cylinder wall surface area, m^2
c	cylinder head clearance, m
c_p	specific heat capacity, $J.kg^{-1}.K^{-1}$
c_s	solid specific heat capacity, $J.kg^{-1}.K^{-1}$
D	store diameter, cylinder bore, m
D_h	cylinder hydraulic diameter, m
d_p	particle diameter, m
G	mass flux, $kg.s^{-1}.m^{-2}$
h	convective heat transfer coefficient, $W.m^{-2}.K^{-1}$
k	thermal conductivity, $W.m^{-1}.K^{-1}$
l	length scale, m
L	store length, con-rod length, m
m	mass, kg
$\dot{m}$	mass flow rate, $kg.s^{-1}$
n	polytropic index, -
N	heat pump/engine rotational speed, rpm
P	gas pressure, Pa, bar; power, W
Q	rate of heat transfer, W
r	crank radius, m
s	stroke length, m
S_v	particle surface area to volume ratio, m^{-1}
T	temperature, K
t	time, s
U_o	Open-tube gas flow velocity, $m.s^{-1}$
V	store volume, m^3
V_s	swept volume, m^3
v_p	piston speed, $m.s^{-1}$
W	rate of work transfer, W

Greek letters

α	loss factor, -; store utilisation factor, -; thermal diffusivity, $m^2.s^{-1}$
β	pressure ratio, -
γ	heat capacity ratio, -
ε	store void fraction, -
ϵ	heat exchanger effectiveness, -
η	polytropic efficiency, -
θ	crank angle, $^\circ$
μ	gas dynamic viscosity, Pa.s
ρ	gas density, $kg.m^{-3}$
σ	screen valve porosity, -
τ	time scale, s; temperature ratio, -
ϕ	polytropic exponent, -
ω	angular frequency, $rad.s^{-1}$

Subscripts

b	packed-bed
c, d	charge; compression, discharge; demonstrator
C, E	compressor, expander
e	electricity-to-electricity
f	flow
g, s	gas, solid
h	heat loss (or gain)
p, m	particle, modified
t	thermal, thermodynamic
u	utilisation
w	cylinder wall

Abbreviations

CB	Carnot Battery
CE, EC	compressor-expander (charge mode), expander-compressor (discharge mode)
HP, LP	high-pressure, low-pressure
HS, CS	hot store, cold store
HX1, HX3	low-pressure heat exchanger, high-pressure heat exchanger
PHES	Pumped Heat Energy Storage
RES	renewable energy sources
RTE	Round-trip efficiency
TES	Thermal Energy Storage

energy dependency on conventional means and address the challenges of energy security and climate change. Reportedly, in compliance with the 2009 EU Renewable Energy Directive (RED), the UK had set a target to producing 15 % of its total final energy consumption from RES by 2020. The UK met this target by sourcing 13.6 % of its total final energy consumption from the renewables [1]. Since the introduction of the EU directive, the deployment of RES has been growing on yearly basis. Following Brexit, the UK presented its Nationally Determined Contribution (NDC) in line with Paris Agreement, according to which the UK is committed to cut carbon emissions by at least 68 % by 2030 compared to 1990 levels [2]. Moreover, the ultimate target set by both the EU and UK is to reach carbon neutrality by 2050. These targets imply that RES are getting significant interest in the research, development and deployment areas in the coming decades to realise clean energy transformation.

RES are characterised by their variable and intermittent nature due to variation in weather patterns. Increasing penetration of RES in the energy network and time mismatch between production and demand have triggered a big challenge to find out cost-effective solutions to store the harnessed energy. Therefore, a storage facility is mandatory to create a bridge between fluctuating energy production and consumption; as such, it must be able to transfer off-peak energy to high demand periods. Many studies and reports have highlighted the paramount need for increasing storage capacities in coming years. For example, a study [3] shows that with 10 GW of wind power, 1200 GWh of storage capacity will be required for a five-day lull in the UK. Moreover, in a report the

International Energy Agency presents a 2DS scenario according to which the global temperature rise is needed to stay below 2 °C by 2050 [4]. It is estimated that the share of RES in power generation will be 34, 44, 33 and 26 % by 2050 in the United States, EU (27 countries), China, and India, respectively. These four major regions currently have a total installed power generation capacity of 1177, 963, 2355 and 470 GW in 2021, respectively [5,6]. To comply with the decarbonisation target, 310 GW of additional grid-connected electricity storage capacity will be necessary in these regions [4]. All these trends and forecasts imply an inevitable rise in the demand for sophisticated electricity storage systems.

A wide array of electricity storage approaches exists which can be categorized as electrical, mechanical, chemical, thermal, magnetic and heat engine based [7]. Chen et al. [8] gave a critical overview and compared technical characteristics of different mature and developing technologies. As of now, Pumped Hydropower Storage (PHS) and Compressed Air Energy Storage (CAES) are commercially available enabling provision of large-scale grid storage. Both PHS and CAES are mature systems and have been successfully adopted as they offer cheap storage solution; capital energy cost for PHS is 5–100 $/kWh and that for CAES is 2–120 $/kWh [9]. However, geographical requirements suggest that both storage systems cannot be employed freely [10]. Other known but relatively premature and less recognised storage systems exist and have been reported in the literature [11,12].

Of the large-scale storage technologies (>100 MWh), Pumped Heat

Energy Storage (PHES) is emerging now as a strong candidate. Electrical energy is stored across two storage reservoirs in the form of thermal energy by the use of a heat pump. The stored energy is converted back to electrical energy using a heat engine. A PHES system undergoes a charge-storage-discharge cycle just like any electrochemical battery storage. However, the electrical energy is stored in the form of thermal energy. Based upon these two aspects this system is analogously known in the scientific community as Carnot Battery (CB) [10,13]. Notably, the ongoing work uses the name 'Pumped Heat Energy Storage' throughout the text instead of an alternative name 'Pumped Thermal Electricity Storage (PTES)' which is commonly found in literature used to refer to the same storage technology [14]. Based on the principle of CB, PHES is being studied or commercially developed using two possible cycle configurations: Brayton and Rankine [15]. For example, Malta Inc. [16] is aiming to develop a commercial-scale 20 GWh Brayton PHES system based on the concept presented by Laughlin [17], which uses molten salt and coolant reservoirs, to support long-duration storage (10–200 hrs). In 2019 Siemens Gamesa [18] started building a 30 MWh Rankine PHES system using 1000 tons of rock fill to provide electricity for up to 24 hrs using steam turbine. Based on conventional thermodynamic cycles, a PHES system can be built with existing industry-proven components. Free from environmental restrictions, use of environment-friendly storage materials and working fluids, low plant footprint, easily deployable nature, and competitive technical performance along with quick response time are the main factors to stimulate its emergence [19–21]. It allows energy to be stored at lower storage pressures (1–12 bar) making it cost-effective intrinsically [22]. Benato et al. [23] pointed out that the cost of storage unit for PHES system is 60 \$/kWh, which is lower compared to that of PHS and CAES. As part of the ongoing demonstration project, Smallbone et al. [24] evaluated Levelised Cost of Electricity Storage for a 16 MWh PHES system, and according to them this cost is only between 2.7 and 5.0 €ct/kWh.

In the present study, a closed Brayton PHES demonstration system was built and tested in Hampshire, UK. This system employs storage reservoirs filled with crushed rock. There are already some publications which theoretically investigate the system of the current form [21,22]. These works deal with simplest form of the system and focus on either parametric optimisations or identification of various losses and their effects on the Round-trip efficiency (RTE). White et al. [21] presented a thermodynamic analysis of the system with focus on sensitivity analysis of the RTE to key losses. The analysis showed that instead of compression temperature ratio, the RTE and storage density both increase with the ratio between the highest and lowest temperatures across thermal stores. McTigue et al. [22] performed parametric optimisations for a hypothetical 2 MW storage system and indicated that about 85 % thermodynamic RTE can be predicted for given optimistic values of the considered parameters. Both studies considered reciprocating type machines to achieve compression and expansion. Wang et al. [25] have also studied the same system but considered a relatively bigger size (10 MW) and considered argon and helium as working gases. Their study indicated that helium yielded higher RTE (56.9 %) compared to argon (39.3 %) due to small resistance losses incurred by helium through thermal stores and heat exchangers. In a following study, Wang et al. [26] discussed the unbalanced mass flow rate of the thermal stores which has been mostly considered as uniform in other studies. A new method was proposed without the use of buffer vessel, however, the RTE was marginally improved (only 0.12 % increase was predicted). Nevertheless, the proposed system was presented as an economically viable option due to reduction in the system's initial cost. Although the PHES system has been studied in the present baseline form there are some studies considered novel modifications to its layout to make it adaptable to certain working conditions. As an instance, Zhang et al. [27] proposed a 10 MW PHES system with indirect thermal energy storage and

highlighted the advantages in terms of low installation cost with minor RTE penalty. Koen et al. [28] presented a system operating on glide cycle using unpressurised water as storage medium. The system enabled very low exergetic losses whilst maintaining high cycle work ratio and producing around 50 % overall RTE. In their latest work, McTigue et al. [29] performed theoretical analysis on the PHES system involving recuperation and using liquid storage tanks instead of packed-beds of rock. The optimal system design was able to achieve RTE in the range 59–72 %. A detailed exergy analysis was performed by Zhao et al. [30] with a similar system layout as in [29]. It was revealed that the expander and cold heat exchanger during discharge yielded highest exergy destruction rates compared with other system components. Furthermore, transcritical and subcritical versions of the Rankine PHES system have also attracted researchers in the past decade [31–33]. Zhao et al. [34] performed an optimisation study which included all three major variants of PHES system based on cycle type, working fluid and storage medium: Brayton PHES with solid packed-beds, Brayton PHES with liquid storage tanks and transcritical Rankine with liquid storage tanks, with the last system showing highest RTE of 68 %.

Main components of the system, especially packed-bed stores, have also been studied and parametrically optimised keeping in view the current version [35–37]. Due to being cost effective and versatile, packed-bed thermal stores have been widely used for heat storage in PHES applications. Anderson et al. [35] studied packed-bed thermal energy storage (TES) and validated the model by conducting experiments. In another related study, Al-Azawii et al. [36] experimentally investigated the thermal behaviour of the packed-bed TES composed of 100 % recycled ceramic storage material under varying conditions of flow rate and cycle durations. Comparison of results with alumina as storage material indicated that alumina yielded superior thermal performance, but pressure losses were higher compared to ceramic. More recently, Esence et al. [37] presented a versatile one-dimensional, three-phase numerical model able to treat different configurations of the packed-beds. The model was validated against different experimental data covering a wide range of operating conditions. The effect of fluid velocity on the thermocline behaviour was investigated and an optimal value to achieve maximum utilisation of the store was revealed. While most studies have considered sensible heat mechanism for thermal stores, another alternative option is also being investigated which employs phase-change materials and the method is known as latent heat storage. Zhao et al. [38] conducted a study on cascaded latent-heat store operating in pure electricity-storage mode as well as combined heating and power (CHP) mode. The results revealed that the store yielded maximum RTE in the range of 62–100 % when operated in CHP mode. Albert et al. [39] investigated a PHES system that involved packed-bed stores in which additional latent storage was utilised to maximise the duration of the high power output.

Previous theoretical studies [21,22] have asserted that the RTE is mainly dependent upon the compression and expansion losses in contrast to the losses within thermal stores which are only a few percent. For example, using optimisation studies, McTigue et al. [22] showed that with 90 % polytropic efficiency, a RTE of 53–58 % can be achieved, which can be increased to 72–87 % with 99 % polytropic efficiency. To act as a heat pump/engine, reciprocating type machines have been considered due to their ability to achieve higher polytropic efficiencies compared to turbomachines. Bespoke reciprocating engine has been theoretically investigated in [40,41]. Willich et al. [40] presented computational study of the thermodynamic losses associated with heat transfer and relying on qualitative results concluded that thermal irreversibility may be the main factor limiting the efficiency of reciprocating machines. The study was further extended in [41], where it was revealed that for a reciprocating machine with uni-flow valve arrangement, mass flow rate and instantaneous heat transfer coefficients are significantly

affected by the discharge pressure and piston speed. Because of the absence of substantial experimental data pertaining to such compressor-expander machines, a study giving an exact value of a system's actual RTE is non-existent. This has allowed the researchers to rely only on assumed values of standard isentropic or polytropic efficiencies [22,42]. Hence, in order to prove the feasibility of such a system as an innovative and alternative solution, it is vital to determine the actual performance of the compressor-expander machine.

1.1. Present work

As aforementioned, so far there is no report on the experimental performance of a fully developed PHES system operating on closed Joule-Brayton cycle concept. The only study which is of significant relevance to the current system with respect to practical point of view is that of Howes conducted in 2011 which is related to a series of experiments performed to develop the heat pump/engine machine only [43,44]. While working with Isentropic Ltd, Howes attempted to develop a prototype heat pump for reversible heat/work conversion based upon first Ericsson cycle and theoretically assessed the potential performance of a large-scale (2 MW) PHES system by extrapolating the results from the heat pump machine in combination with two hypothetical thermal stores. Around the same time, a patent was published by SAIPEM SA based upon similar energy storage concept [45] which was also studied but only theoretically by Desrues et al [46]. Because of lack of commercial interest and investment, energy storage using PHES technology did not receive as much attention in the past. However, the technology has seen dramatical rise in interest recently due to urgency in meeting the global carbon-free futuristic targets. Therefore, the aim of present work is to address this important issue by evaluating the performance in terms of thermodynamic Round-trip efficiency (RTE_t) of the world's first grid-scale 150 kW_e PHES demonstration system built and commissioned recently. The demonstrator employs the improved design of heat pumping device developed by Howes (with some additional modifications after rigorous research and testing) to work as heat pump/engine in the current system. In addition, the demonstrator employs two advanced packed-bed type thermal stores to provide necessary thermal energy storage. Basically, the demonstrator has been developed as a 'scaled validation system' for necessary testing of the several novel concepts employed in the system components and to provide strong basis for an 'up-scaled' system implementation at a grid or substation level to supply necessary storage. This paper presents only the crucial technical details of the demonstrator components which are of significant interest with respect to thermodynamic point of view. This study comprises of both experimental work and subsequent numerical analyses for overall thermodynamic performance assessment. In the experimental part of the study, the system was operated at part-load (or under-design) conditions due to incurred valve flow leakages within the heat pump/engine at higher pressures. Therefore, complete storage cycle at full-load (or design) conditions was only possible to be evaluated using simulation at this stage. The main novelty of the present work lies in identifying actual performance of the compressor-expander machine (serving as heat pump/engine) by using the preliminary experimental data taken from the demonstrator. The experimentally validated performance of the compressor-expander machine is, therefore, used to confidently predict the RTE of a complete storage cycle over a wide range of operating conditions (from part-load to full-load conditions). A mathematical model which includes transient operation of the thermal stores is developed for this purpose. The model for thermal stores was validated in a separate experimental study and has not been included here. Lastly, using the developed mathematical model, the current investigation is further extended to include the influence of cyclic behaviour of the thermal stores on the RTE of the demonstrator.

The rest of the paper is organised as follows: Section 2 describes the demonstrator, its main components and data measurement technique, Section 3 presents mathematical modelling of main components which

is followed by Section 4 on experimental results and discussion. At the end, in Section 5, the simulation results of complete system operation are presented.

2. Description of the demonstrator

Fig. 1 shows main parts of the demonstrator. The system consists of four main components: a hot store, HS, a cold store, CS, a compressor, C, and an expander, E. The interchangeable compressor and expander act as a reversible heat pump/engine to compress and expand an inert working gas. To compensate losses in reversibility incurred during heat and work transfer processes, four subsidiary components are implemented: a low-pressure heat exchanger, HX1, a high-pressure heat exchanger, HX3, a buffer tank, B, and an electric heater, H. Besides, a synchronous motor-generator, MG, is required for the inter-conversion of electrical and mechanical energies. The stores contain a refractory material such as mineral (crushed gravel) and are connected to each other through the pump/engine. The pump/engine is responsible for creating pressure and thermal potential difference across the stores. The schematic highlighting system's basic layout is shown in Fig. 2. Arrows in the figure indicate a charge cycle. The sharp hot and cold thermal fronts can be seen moving up and down the stores as the working gas heats and cools the HS and CS respectively.

2.1. Working principle

The working principle of PHES is highlighted here briefly for completeness as it has been exposed in other papers in detail (see, for example, [19,22,43,46]). The process consists of charge, storage and discharge periods. During charge the system uses electrical energy taken from the grid (or directly from the renewables) to drive the MG which operates the (electricity-driven) heat pump working on the reverse Joule-Brayton cycle. The cycle follows the route 1a–2–3–3a–4–1, as shown in Fig. 2. The heat pump/engine operates as a compressor-expander, CE, device. The working gas is compressed through C to a high temperature and pressure and is fed into the HS (state 2) where it transfers its heat to the storage media. The gas exits the HS (state 3) and is further cooled down to the high-pressure datum temperature through HX3 (state 3a). The gas is then expanded through E to a low temperature and pressure and is fed into the CS (state 4) where it cools the storage media. The gas exits the CS (state 1) and is further heated up to the low-pressure datum temperature through HX1 (state 1a). Electrical energy is thus stored in the form of thermal energy in the storage media. During discharge the system uses the stored thermal energy to drive the MG which operates the (heat-and-cold-driven) heat engine working on the standard Joule-Brayton cycle. The cycle follows the same route but in reverse. The same heat pump/engine operates as an expander-compressor, EC, device now. Concisely, the working gas receives heat from the HS, undergoes expansion through E, gives heat to the CS and finally undergoes compression through C. The stored thermal energy is thus converted back to electricity. T-s diagram representing the charge cycle of a PHES system is shown in Fig. 3.

2.2. Thermal stores

Heat and cold are stored in thermally insulated, isobaric steel containments. Both HS and CS of the present PHES system are 'packed-bed' type storages. Packed-beds are loosely packed with a particulate storage material normally spherical in shape to allow for working fluid flow for effective heat transfer. Such packed-beds have been widely used in different engineering systems and the flow behaviour is often investigated in the name of 'flow through porous media'. Chemical industries frequently involve processes where packed- or fluidised-beds are commonly used. Waste heat recovery, catalytic reactors and food processing plants often use the characteristics of packed-beds which are suitable for TES.

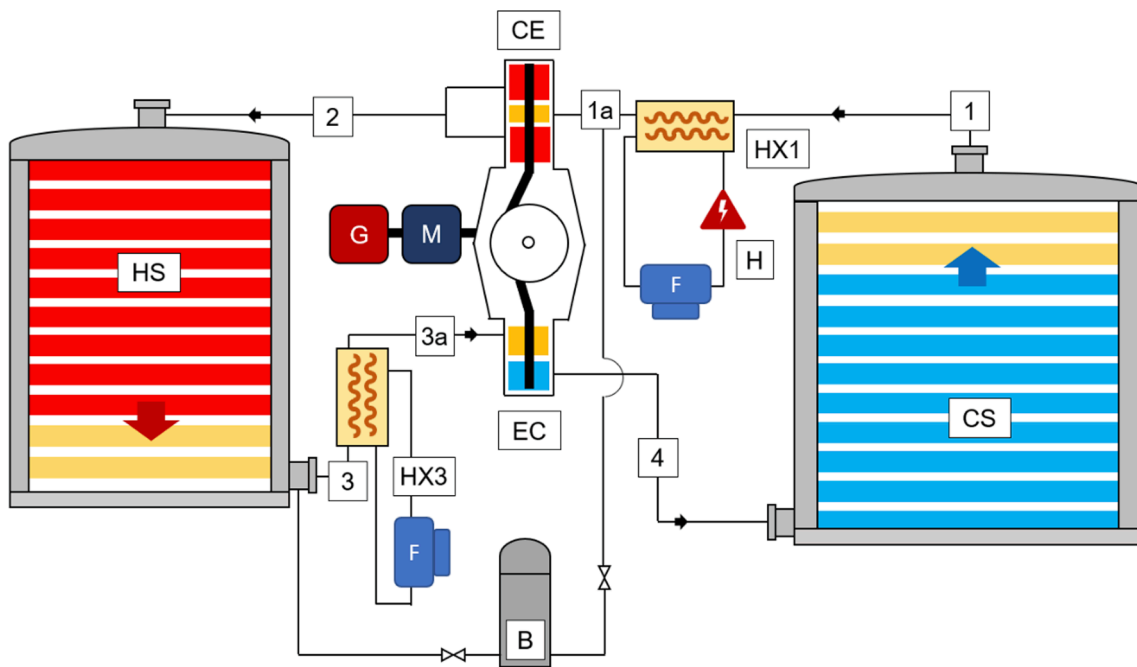**Fig. 1.** 150 kW$_e$ PHES demonstrator built at Hampshire, UK.

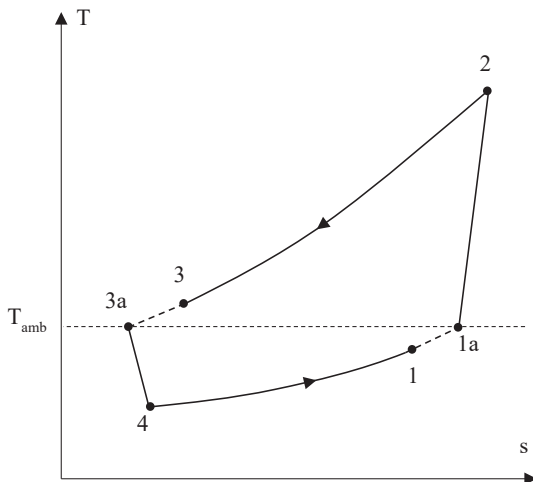**Fig. 2.** Basic layout of PHES demonstrator (not to scale).

Fig. 3. T-s plot of a PHES process during charge.

Magnetite pebbles[1] with a diameter range of 1.4–2.8 mm were used as the storage media in the stores. Both HS and CS are made up of several layers of the storage media, as shown in Fig. 4. The figure shows part of the HS during charge where gas flows from the top and is blown over the media layers. The layering (or segmentation) concept in the packed-beds for TES applications is fairly new and has been patented prior the development of the demonstrator [44] (Further detailed technical description can be found in another patent [47]). Control of the thermal front through the stores is achieved by opening (or closing) of multiple gas bypass choke valves positioned around the edges of each media layer. An intelligent layer control system is employed to open (or close) the valves using pneumatic valve actuation mechanism. The opening or

---

[1] Magnetite is naturally soft and therefore it was fired with a graded material to harden the surface to be able to survive successive cyclic thermal loads. There is a small amount of silica present in magnetite (14% by volume) but our analysis shows that it does not make much difference. Assuming nearly spherical shapes, an average equivalent particle diameter is assumed for use in the thermal store model.
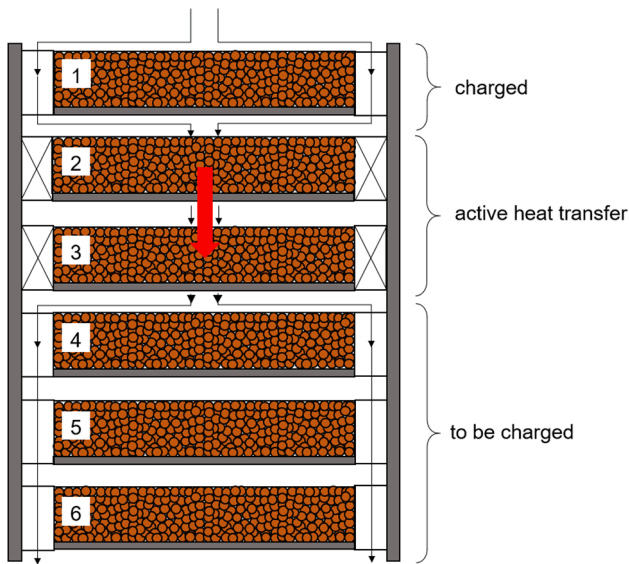
Fig. 4. Schematic diagram of a layered store. Thermal front is limited to layers 2 and 3 only.

closing of valves depend on the solid or gas temperature set point. Gas flow is directed through open valves to avoid media and is blocked by closed valves to direct the gas to the selected layers being charged or discharged (see Fig. 4). The layered structure serves two purposes in enhancing storage performance. Firstly, with controllable valves and peripheral flow bypass, layers that are not actively heated or cooled are effectively bypassed thereby enabling narrow 'thermocline' behaviour. And secondly, pressure losses (particularly in the CS) are reduced during operational periods. These trends have been observed in the present study but not discussed here (see work carried out by White et al. [48]). Both stores employ a filter at the top and bottom to prevent any debris from going into the pump/engine. The filters are in the form of a tray made up of metallic frame to hold the filtration paper in place. The frame is made up of fabricated stainless steel and a pleated filtration paper having a pore size of 20 μm is used together with Cadisch Hollander Mesh 165/800. The mesh filters operate with a pressure drop of less than 100 Pa at a maximum flow rate of 1.43 kg/s using argon as working gas. Additionally, the stores are internally insulated to prevent any undesired thermal loss and keep the surface temperatures below design limit. Key details of the stores are given in Table 1.

2.3. Reciprocating heat pump/engine

The demonstrator system uses a novel reciprocating type dual-purpose machine which employs a number of advanced concepts to realise as near a reversible heat pump/engine. The machine consists of one double-acting-piston cylinder (working as compressor/expander during charge/discharge) and one single-acting-piston cylinder (working as expander/compressor during charge/discharge), both forming a single unit. The general configuration is shown in Fig. 5. Compared to rotary turbomachines, this type of machine provides a cost-effective solution for PHES applications. By varying valve timing instantly, the cylinders acting as compressors during charge can work as expanders during discharge and vice versa; the need for more components is thus avoided. In addition, this helps to switch between the charge and discharge modes quickly without having to change the direction of rotation of the machine. Geometric details of the pump/engine are given in Table 2. It is to be noted that a bore-to-stroke ratio of 4 (which is quite different from conventional engine proportions) ensures improvement in efficiency due to reduced piston speed which is dynamically linked to various losses (e.g., liner friction, turbulence and pressure drop). (See details in Refs. [43,47]).

Table 1
Specifications of thermal stores.

Packing material	86 % Fe_3O_4, 14 % SiO_2	
Average density, ρ [kg.m^{-3}]	4800	
Equivalent diameter of particles, d_p [mm]	2.1	
Void fraction, ε [–]	0.425	
Stores	HS	CS
Energy storage density[a], ρ_{ES} [MJ.m^{-3}]	1123	488
Length[b], L [m]	2.676	2.505
Diameter, D [m]	2.194	2.998
Total volume, V [m^3]	10.117	17.683
Packing material amount, m_s [ton]	18.5	32.4
Number of layers	16	15
Allowable flow rate, $\dot{m}_g$ [kg.s^{-1}]	0.6–1.43	

[a] $\rho_{ES} = m_s c_s(T)\Delta T/V$ is computed with respect to assumed initial conditions given in Section 5 by considering volume formed by the packing material only i.e., excluding the volume required for layer shelves and gas gaps.

[b] This is the overall length of the store which consists of a vertical material depth of 111 mm, shelf thickness of 24 mm and a gas gap of 36 mm for each layer of the store.
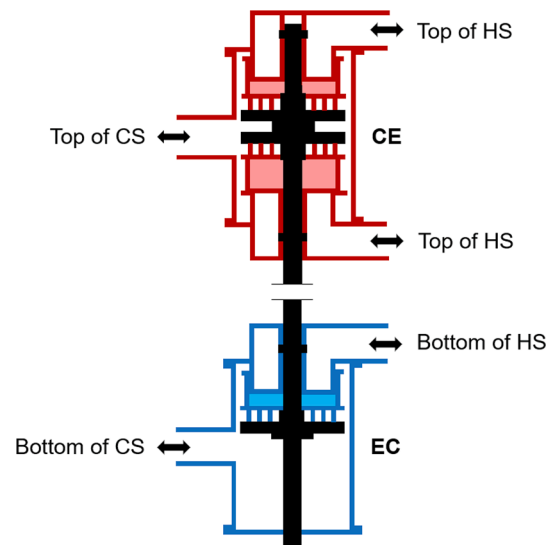

Fig. 5. Heat pump/engine layout.

Table 2
Specifications of heat pump/engine.

Cylinder bore, D [m]	0.4
Stroke, s [m]	0.1
Crank radius, r [m]	0.05
Con-rod length, L [m]	0.322
Head clearance, c [m]	0.007
Polytropic efficiency, η [–]	0.98
Speed range, N [rpm]	250–1000

2.4. Heat exchangers

The PHES system is adiabatic and reversible, at least in ideal situation. But with each main component deviating from ideal behaviour, any residual irreversibility generates some waste heat. Such heat will keep on building over successive storage cycles unless, in case of a closed cycle, it is removed from the working gas, ideally at the lowest available temperature (here at points 3 and 1 in Fig. 2). In the present case, heat exchanges are required to maintain a constant inlet temperature for the compressor and expander during charge and thermal stores during discharge.

Each heat exchanger system employed in the demonstrator is a two stage (consisting of an internal and an external heat exchanger), single pass and counter-flow type. The internal heat exchangers are housed within the stores which are connected to the external air-cooled heat exchangers. (Note that for brevity, only external heat exchangers are shown in Fig. 2). As the thermal fronts emerge at the exit to any store, the temperature of working gas entering the heat exchanger section changes which requires different cooling rates. This is achieved by variable speed fans. Table 3 presents key specifications of the two heat exchanger systems. Additionally, a 9-kW electric heater is used within the circuit of HX1 to get a greater control of CS temperatures to achieve required system pressure ratio.

2.5. Gas buffer

A fixed volume storage vessel known as gas buffer was used to contain and supply access working gas mandatory for proper functioning of the demonstrator. When the system is charged after a fully discharged state, the total mass of the working gas in the system will change subject to changes in the thermodynamic states, e.g., gas density, at different temperatures and pressures. In order to maintain mass balance of the system, during charge, gas is transferred from the HP ambient condition (point 3 on Fig. 2) to the buffer, and during discharge, from buffer to the LP ambient condition (point 1 on Fig. 2). Table 4 contains specifications of the buffer system.

Total volume required for buffering is estimated by calculating the maximum and minimum working gas masses around the whole system and subtracting one from the other. An illustrative example is shown in Fig. 6 indicating the transient variation of total gas mass within the HS and CS only for first simulated storage cycle at full-load with reversible adiabatic heat pump/engine (Section 5.1). A mass difference of ~72 kg would mean that at HP datum temperature and 6 bar pressure, an additional volume of ~7.7 m^3 will be required to be available between points 1 and 3 on the schematic diagram. A note should be made here that the computed value of additional volume required is lower than the design value (stated in Table 4) because the calculations were performed using the transient store model which only takes into consideration the gas volume present in the voids of the storage medium. In practice, under extreme conditions, the required volume would be higher as some quantity of the gas will also be present in other parts of the system, such as thermal store plenums, inter-layer gaps and manifolds connected to the heat pump/engine. The system's main controller commands an intelligent buffer control system for necessary action throughout the storage cycle when required to maintain mass balance across the system. The simulation model, therefore, assumes a uniform mass flow rate at the inlet and exit to any component. Interestingly, Fig. 6 shows that the total gas mass drop across the stores during charging and rise during discharging is not smooth, as the presence of spikes on the charge and discharge curves. This behaviour is because of the thermal front control strategy (described in Section 3.1) and is associated with the control system implemented specifically for the layered stores. As an instance, once a particular layer has charged or discharged, the layer control system deactivates it and activates next layer in line according to the set criteria. This results in gas temperature suddenly change at the active layer exit leading to change in local gas density and thus the gas mass.

Table 3
Specifications of heat exchangers .

	HX1	HX3
Service fluid	Duratherm LT thermal oil	20 % propylene glycol/water mix
Flow rate, V [L.s^{-1}]	1.2	1.4
Working pressure, P [bar]	1.0	1.5
Overall effectiveness, ϵ [–]	0.5	0.5

Table 4
Specifications of buffer system.

Buffer type	Working pressure range	Working temperature range	Total volume
Air receiver	1–12 bar	−5 to 35 °C	15.24 m^3
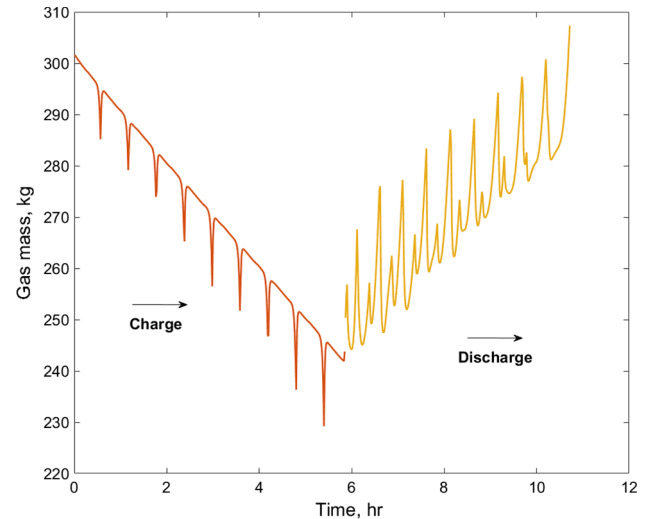
Fig. 6. Variation of total gas mass within stores for first storage cycle. The temporary spikes in the curves are because of front control and operational requirement of the layered stores.

The analysis of results shows that the spikes are pronounced particularly because of gas variation in the cold store, this is due to cold store is operated at lower pressure and temperature than the hot store. It should be noted that such sharp variations in gas temperature and mass in stores will not affect the performance of the heat pump/engine and thus the power input/output during charging/discharging. For a smooth operation, this feature exhibited by layered stores is mitigated by employing two external heat exchangers and the buffer system. A robust integrated control system identifies any variations and ensures nearly constant mass flow rate and temperature of the working gas. During discharge, these fluctuations are further smoothed due to mechanical inertia of the flywheel present at the crankshaft.

2.6. Data acquisition

Experimental data was recorded from the demonstrator using thermocouples, pressure and torsional measurement sensors fixed at various points of the system, details of these sensors are presented in Table 5. For temperature measurements, *N*-type and *T*-type thermocouples are employed. The *N*-type are used in HS layers, CE exit and EC inlet manifolds whilst the *T*-type are used in CS layers, EC exit and CE inlet manifolds. Kulite pressure sensors are employed for pressure measurements. CE cylinders and connecting inlet and exit manifolds employ pressure sensors dedicated for high temperature range whilst EC cylinder and connecting inlet and exit manifolds employ cryogenic type sensors. Piston displacement is measured using a high-speed linear magnetic encoder. Measurement data is collected at 25 kHz sampling rate and logged using Citadel database of National Instruments.

3. Mathematical modelling

This section describes the mathematical modelling required in the simulation phase of ongoing study. As the demonstrator was operated at part-load conditions with focus on reciprocating pump/engine testing

Table 5
Data measurement.

Sensor	Measurement range	Measurement accuracy
Kulite cryogenic (−195.5 to + 120 °C)	0–17 bar 0–3.5 bar	±0.5 % FSO (Max.)
Kulite high temperature (−55 to + 538 °C)	0–14 bar 0–3.5 bar	
N-type thermocouple	0 to + 1100 °C	±1.5 °C (−40 to +375 °C) ±0.004 T °C (375 to 1000 °C)
T-type thermocouple	−185 to + 300 °C	±0.5 °C (−40 to +125 °C) ±0.004 T °C (125–350 °C)
LM10 linear magnetic encoder	50 m (Max.)	±20 μm/m

only, prediction of the system overall performance at full-load conditions was realised by necessary modelling of the main components and carrying out simulations. The thermodynamics and relevant heat/work transfer mechanisms involved in the storage cycle have been modelled based on widely accepted and previously established models. Experimental data specific to the pump/engine performance has been validated and analysed keeping in view the noteworthy work by Howes [21] and used in the simulation runs. The model includes use of the temperature-variant thermophysical properties of the working gas to cover a wide range of pressures and temperatures involved in the cycle. This is achieved by using a database, REFPROP 9.1 [49], linked with MATLAB.

Round-trip efficiency (RTE) is taken here as the main performance metric, given as the ratio of the discharged work to the work required for charge.

$$RTE = \frac{W_{discharge}}{W_{charge}} \qquad (1)$$

Maximum RTE is limited by the irreversibility of each process of the thermodynamic cycle. Ideally, in the absence of irreversibilities, 100 % efficiency is achievable. Practically, the RTE is always lower due to various losses taking place in the system components. These have been identified and mentioned in the modelling scheme presented below.

3.1. Thermal stores

The modified version of well-recognised Schumann model [50] for a 2-phase, 1-D case of packed-bed TES has been used here to quantify gas–solid[2] heat transfer with following assumptions.

- The radiative and conductive heat transfers (between solid particles, layer shelves and store walls) are assumed to be negligible and the model only accounts for the convective mode of heat transfer. Circumferential and radial temperature distributions have also been ignored ascribing to predominant variation along vertical axis only (1-D case);
- Nearly zero Biot number is considered which reflects minimal heat transfer resistance inside the solid particles, which suggests each particle carries uniform temperature field;
- Heat leakage through walls to the external, ambient conditions is ignored by current study due to the presence of a high level of insulation surrounding the stores;
- The mandatory gas gaps (or dead space) present between successive layers do not yield any thermal or pressure loss; for calculations, an

---

[2] From here onwards, storage material will be called solid and working fluid will be called gas for simplicity.

effective length of the bed is, therefore, used which is made up by the depth of all solid layers combined.

The solution of the governing equations needed to quantify transient response of the stores considers a new, efficient semi-analytical approach first presented by White [51]. This is essentially based on the methods of Wilmott [52].

Considering an infinitesimal control volume, as shown in Fig. 7, the heat transfer rate between gas and solid is given by

$$\delta \dot{Q} = h \delta A \left(T_g - T_s \right) \qquad (2)$$

where

$$\delta A = A_b \delta z (1 - \varepsilon) S_v \qquad (3)$$

Here ε is void fraction, defined as $\varepsilon = V_g / V_b$, and $S_v = 6/d_p$ is the particle surface area to volume ratio. The mass continuity equation for the control volume is given as

$$\varepsilon \frac{\partial \rho_g}{\partial t} = \frac{\partial G}{\partial z} \qquad (4)$$

where G is the open-tube mass flux defined as $G = \rho_g U_0$. Applying unsteady flow energy equation to the gas, together with Eq. (4), gives a fundamental differential equation of the form [51,53]

$$\dot{m}_g c_p \frac{\partial T_g}{\partial z} \delta z + \left(\delta m_g c_p \frac{\partial T_g}{\partial t} - \delta V_g \frac{\partial P}{\partial t} \right) = -\delta \dot{Q} \qquad (5)$$

The second term in above equation on the left side represents the rate of accumulation of energy by the gas and is derived including unsteady mass continuity equation.

Performing an energy balance on the solid yields

$$m_s c_s \frac{\partial T_s}{\partial t} = \delta \dot{Q} \qquad (6)$$

Defining length scale as $l = \dot{m}_g c_p \delta z / h \delta A$ and time scale as $\tau = \rho_s c_s / h S_v$, the normalised form of the two equations for gas and solid become

$$\frac{\partial T_g}{\partial z} + \frac{\varepsilon \rho_g}{G} \frac{\partial T_g}{\partial t} - \frac{\varepsilon}{G c_p} \frac{\partial P}{\partial t} = \frac{\overline{T}_s - T_g}{l} \qquad (7)$$

$$\frac{\partial T_s}{\partial t} = \frac{\overline{T}_g - T_s}{\tau} \qquad (8)$$

These differential Eqs. (7) and (8) can be solved by finite volume-time progression approach to track the hot and cold thermal fronts. The details of above formulation and related computational method have been presented in [51,53], and for brevity, are not mentioned here.
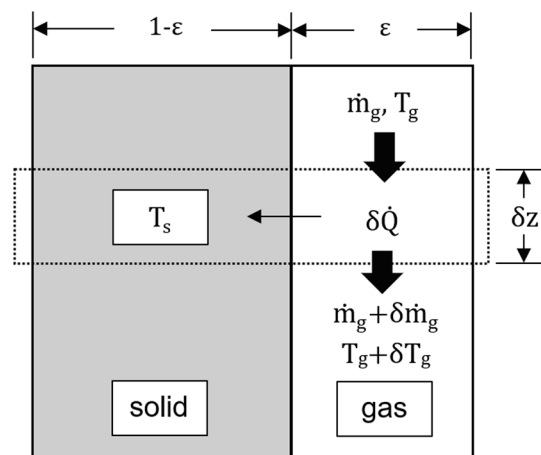
Fig. 7. Control volume depicting gas–solid heat transfer.

The convective heat transfer coefficient is given by $h = Nuk/d_p$ and the required Nusselt number correlation suggested by Wakao et al. [54] is considered here

$$Nu = 2.0 + 1.10(Pr)^{\frac{1}{3}}(Re_p)^{\frac{3}{5}} \tag{9}$$

where $Re_p = Gd_p/\mu_g$ is the particle Reynolds number. Many studies point out that pressure drop across the store length is usually only a few percent and does not influence the storage performance to any noticeable extent. However, precise calculations (specially to see how a layered store benefits from this) need both Eqs. (7) & (8) to be solved in conjunction with pressure drop at each point through time and 1-D space. Pressure gradient is determined from Eq. (10) given as

$$\frac{\delta P}{\delta z} = \frac{G^2 S_v (1-\varepsilon) C_f}{\varepsilon^3 \rho_g} \tag{10}$$

where C_f is friction factor. The flow regime in a store is turbulent due to high Reynolds number (reported in Ref. [51]) and hence we can simply use Carman correlation [55] ascribed to turbulent conditions ($Re_m > 2$) of flow to find out friction factor given as

$$C_f = \frac{5.0}{Re_m} + \frac{0.4}{Re_m^{0.1}} \tag{11}$$

where Re_m is the modified Reynolds number and is defined as $G/(1-\varepsilon)S_v\mu_g$.

The model also includes a special strategy required for the controlled movement of thermal front across the length of the layered stores. During charge of HS, top layer charges first and the thermal front gradually moves down to the bottom layer whereas during charge of CS, bottom layer charges first and the thermal front gradually moves up to the top layer. The direction of the thermal fronts is reversed during discharge of both stores.

Consider that T_c and T_d are the temperatures at which a store is charged and discharged, and ΔT is the temperature difference between these two temperatures i.e., $\Delta T = T_c - T_d$. Then, for HS during charge, next layers at the leading edge of the front are actuated when the temperature difference between the temperature of gas exiting the previous layer and T_d exceeds 10 % of the overall temperature rise i.e., $T_{g,e} - T_d > 0.1\Delta T$. Similarly, previous layers at the trailing edge of the front are deactivated when the temperature difference between the increasing temperature of the gas exiting the previous layer and T_d exceeds 90 % of the overall temperature rise i.e., $T_{g,e} - T_d > 0.9\Delta T$. For CS during charge, next layers at the leading edge of the front are actuated when the temperature difference between the decreasing temperature of the gas exiting the previous layer and T_d falls below 15 % of overall temperature drop i.e., $T_{g,e} - T_d < 0.15\Delta T$. Similarly, previous layers at the trailing edge of the front are deactivated when the temperature difference between the decreasing temperature of the gas exiting the previous layer and T_d falls below 85 % of overall temperature drop i.e., $T_{g,e} - T_d < 0.85\Delta T$.

Same approach is applied during discharge; however, the inequality symbols are just reversed. Moreover, as the two stores may not charge (or discharge) at the same time, it is considered that if one of the two stores charges (or discharges) earlier than the other, the numerical model will stop the cycle immediately. This is to avoid excessive heat loss in the heat exchangers.

3.2. Reciprocating heat pump/engine

Both compression and expansion processes have been modelled on the basis of 'polytropic' efficiency instead of classical, standard isentropic efficiency. The latter efficiency is reported to be suitable for (adiabatic) turbomachines due mainly to observed internal heating of the gas because of interaction/friction with vanes [43]. In case of a reciprocating machine, keeping viscous effects, valve pressure losses and

turbulence aside, the non-ideal behaviour is caused primarily due to periodic, parasitic heat exchange between the gas and cylinder walls during compression and expansion due to the relatively longer residence time. For a compressor, this eventually leads to reduced temperature after compression in contrast to what would be in case of an isentropic compression at identical pressure ratio. Some research works also use polytropic efficiency for turbomachines but the efficiency only accounts for thermal irreversibility [56]. However, other researches (see Refs. [22,57]) consider a more thorough definition of polytropic efficiency for reciprocating machines in that there is a distinguished quantification of both heat transfer and irreversibility effects (both being treated simultaneously). The polytropic relations of the following form are used [57].

$$\tau_C = \beta_C^{\phi_C} \text{ with } \phi_C = \frac{\gamma-1}{\gamma}\left(\frac{1-\alpha_{h,C}}{\eta_C}\right) \text{ for compression process}$$

$$\tau_E = \beta_E^{\phi_E} \text{ with } \phi_E = \frac{\gamma-1}{\gamma}\eta_E(1-\alpha_{h,E}) \text{ for expansion process} \tag{12}$$

where τ and β are temperature and pressure ratios respectively. α_h is heat loss (or gain) factor and η is polytropic efficiency. In the current analysis a polytropic efficiency of 98 % is considered which has been reported for reciprocating machines in literatures such as [22,57,58]. This is quite optimistic value and as such would depend on operational conditions, however, a value of 90 % is also considered in some studies with the intent to perform optimisations considering a reasonable range. Nevertheless, keeping in view the special design of the pump/engine a value of 98 % is not beyond scope. An experimental study clearly needs to be conducted in this regard to determine compression and expansion efficiencies based on Eq. (12), with focus on quantifying the two effects separately and their interplay. It should be noted that valve pressure losses also play an important role in dictating compression and expansion efficiencies. In the present analysis, these are treated separately i.e., external to the compression and expansion processes for convenience.

3.2.1. Cylinder heat loss

To determine the value of α_h the parasitic in-cylinder heat transfer phenomenon has been examined by using two approaches. The first approach consists of analysing the experimental data using Howes' correlation [43] and scaling method. The second approach uses several conventional heat transfer models developed over the years for compressors and internal combustion engines. It is a fact that none of the models developed so far is able to fit to all situations that present reciprocating piston-cylinder machinery is used. Despite this such models are still used to gain deeper understanding of the heat transfer phenomenon which governs the machine performance. In the preliminary work, which motivated the design of the current heat pump/engine, Howes [43] conducted experimental tests to build a 'reversible' heat pumping device. Results from their second prototype provide basis for the evaluation of cylinder heat loss (or gain) in this study. An empirical correlation, as shown in Fig. 8, was obtained which inversely relates fractional heat loss factor, α_h, with machine speed, N. α_h is defined as the temperature loss due to irreversibility divided by the isentropic (reversible adiabatic) temperature rise over the same pressure ratio. For a compression process between points 1 and 2, it may be given as [57]

$$\alpha_h = \frac{Q_{poly}}{W_{isen}} = \frac{T_{2s} - T_2}{T_{2s} - T_1} \tag{13}$$

The coinciding measured and ideal plots on the figure (left) indicate that the optimised heat pump/engine design results in a substantially isentropic process. Therefore, because of similar context and approach, and use of the same type of heat pump/engine technology as used in the current system, the correlation obtained by Howes is used here for validation of results. To provide an indication of how current device will behave, an appropriate scaling was applied before using the correlation, as given in Eq. (A6) in Appendix A. The scaling is necessary to make
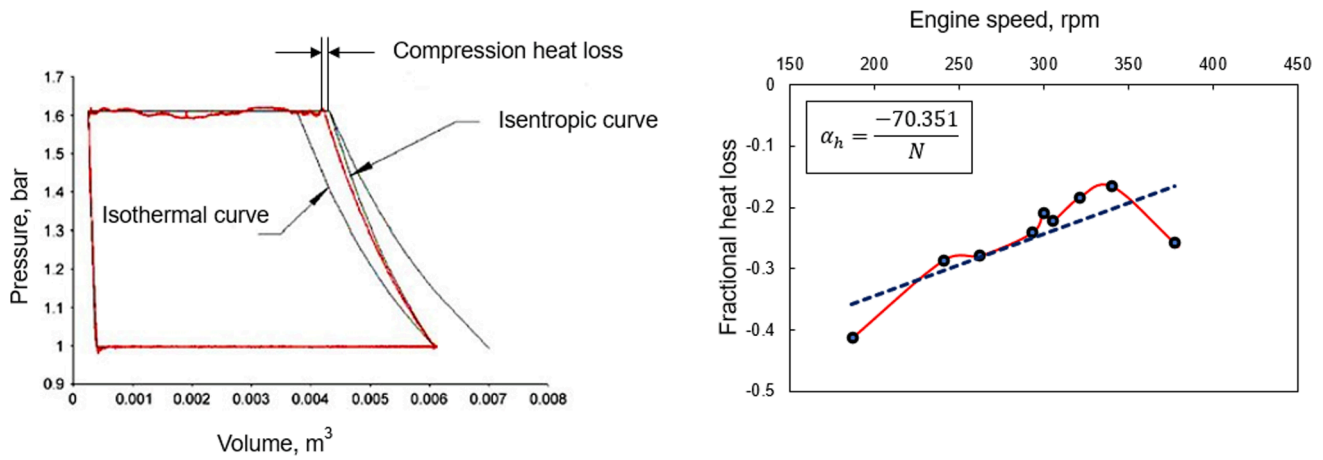
Fig. 8. Comparison of experimental and theoretical P-V diagrams (left). Fractional heat loss vs pump/engine speed (right) [43].

correct allowance for working speed, temperature range, machine size and working fluid properties. This method is described in Appendix A.

Notable conventional correlations for the cylinder heat loss, which are widely (and usually) used as a first choice, are those such as given by Woschni [59] and Annand et al. [60,61]. Many other studies demonstrate the effect of heat transfer on so called gas-spring performance and describe the gas-wall heat exchange quantified by Peclet number, such as [41,62–65]. The rate of instantaneous cyclic convective heat flux at the cylinder wall is given by $\dot{q}_w = \dot{Q}_w/A_w$ where A_w is the internal surface area composed of cylinder side-walls, head and piston faces. Although the in-cylinder heat transfer is studied using the same Newton's law of cooling, the representative models differ based on Nusselt number correlations. In this study, four such models, developed by Kornhauser et al. [63], Lekic [64], Annand et al. [61] and Lawton [66], have been considered for further verification of experimental results. Kornhauser et al. conducted experiments on a gas spring to predict heat transfer behaviour for compressors. Using experimentation and CFD analysis, Lekic modified the correlation given by Kornhauser et al. which provided a better fit to the experimental data. They both used a complex Nusselt number approach as follows

$$\dot{q}_w = \frac{k}{D_h}\left[\mathrm{Nu}_r(T_g - T_w) + \mathrm{Nu}_i\frac{1}{\omega}\frac{d(T_g - T_w)}{dt}\right] \tag{14}$$

The need for a complex Nusselt number arises from the fact that wall heat flux is out of phase with the gas-wall temperature difference. Many recent studies can be found which implemented this correlation for further experimental and CFD-based theoretical investigations enabling a further understanding of heat transfer phenomenon in cases where mass leakage is pertinent, such as [65]. Annand and Lawton performed experiments on internal combustion engines without fuel injection to avoid combustion. The later investigator modified the quasi-steady correlation presented by the former to allow for unsteady heat transfer. On the contrary, they used simple Nusselt number approach as follows

$$\dot{q}_w = \frac{k\mathrm{Nu}}{D_h}(T_g - T_w) \tag{15}$$

Table 6 summarizes the selected Nusselt number correlations. Further collective details of these can be found in review studies, such as [67].

In above equations D_h is the instantaneous hydraulic diameter, given as $D_h = 4V/A_w$, which can be calculated using common piston-cylinder reciprocating machine equations. ω is the angular frequency and T_w is the wall temperature which is assumed constant at 300 K (equal to the inlet manifold conditions) in accordance with common practice where temperature variations within cylinder walls are ignored. Pe_ω is the

Table 6
Nusselt number correlations used in this study.

Studies	Apparatus	Correlations
Kornhauser [63]	Compressor as a gas spring with helium, hydrogen, nitrogen, and argon	$\mathrm{Nu}_r = \mathrm{Nu}_i = 0.56\mathrm{Pe}_\omega^{0.69}$; $\mathrm{Pe}_\omega = \frac{\omega D_{h,0}^2}{4\overline{\alpha}}$
Lekic [64]	Compressor as a gas spring with helium	$\mathrm{Nu}_r = 1.33\mathrm{Pe}_\omega^{0.56} + 5.36$; $\mathrm{Nu}_i = 2.04\mathrm{Pe}_\omega^{0.46} - 1.46$; $\mathrm{Pe}_\omega = \frac{\omega D_{h,0}^2}{4\overline{\alpha}}$
Annand [61]	Internal combustion engine with air	$\mathrm{Nu} = 0.3\mathrm{Re}^{0.7} + \left(1 + 0.27\frac{D}{\mathrm{v}\Delta T}\frac{dT}{dt}\right)$; $\mathrm{Re} = \frac{\mathrm{v}D}{\nu}$
Lawton [66]	Internal combustion engine with air	$\mathrm{Nu} = 0.28\mathrm{Re}^{0.7} - \frac{2.75LT_w}{T_g - T_w}$; $L = (\gamma - 1)\frac{dV}{Vdt}\sqrt{\frac{D^3}{\alpha_0\overline{v_p}}}$

Peclet number which is characterised by using geometry and angular frequency as stated in the table. $D_{h,0}$ is the mid-stroke hydraulic diameter, $\overline{\alpha}$ and α_0 are the cycle-averaged and inlet-conditions based thermal diffusivity of the working gas and L is the compressibility factor.

3.2.2. Valve pressure loss

The heat pump/engine benefits from the application of novel screen valves first proposed by Howes [43]. The mechanical design of these valves was further improved in a separate experimental study by the authors of the present work for use in the demonstrator [68]. The speciality of these valves is that they are placed within the cylinder head and piston to full size of the cylinder bore, hence, enable a uniflow configuration as shown in Fig. 9. The valve geometry is in the form of thin metal sheets comprising an array of rectangular mini ports which offer increased porosity (about 30 % of the bore area) and cause evenly distributed small-scale eddies resulting in improved performance. Quasi-sliding movement of the valve foil opens/closes the ports in the seat thereby unblocking/blocking gas flow. Valve dynamics play a critical role in determining the reversibility of any compression or expansion process. An unsteady, transient flow model is necessary to predict the pressure drop across such a valve. Here, the pressure drop is estimated by assuming each port to be a small orifice. With gas flowing at the speed of piston, the pressure drop is given by the dynamic head loss given below [14,22,57]

$$\delta P = \frac{1}{2}\rho v_p^2\left(\frac{\sigma\sigma_{vc} - 1}{\sigma\sigma_{vc}}\right)^2 \tag{16}$$
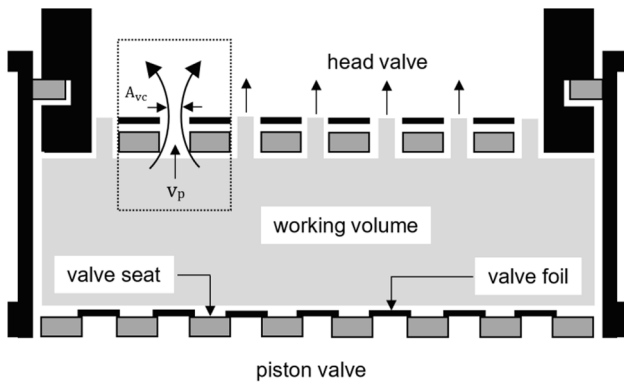
Fig. 9. Uniflow configuration of one of the pump/engine cylinders.

where v_p is the piston speed, ρ is local gas density, σ is valve porosity and $\sigma_{vc} = A_{vc}/A_v$ corresponds to vena contracta effect having a value of ~0.64 [14]. An average pressure drop value can be obtained by integrating the instantaneous pressure drop over the valve 'open' interval. However, it is feasible to consider a rather conservative value here i.e., by evaluating pressure drop at maximum piston speed, which, according to McTigue [14], is slightly higher but does not differ much from the actual estimated loss. Once valve pressure losses are calculated using given conditions, the numerical model adjusts the working gas pressure accordingly and maintains it at the stores' inlet during charge and discharge. Valve pressure losses are further addressed along with cylinder heat loss in Section 4.3.

3.3. Heat exchangers

Performance of heat exchangers is governed by effectiveness of the heat transfer process using a standard equation of the form

$$\epsilon = \frac{Q_{act}}{Q_{max}} \tag{17}$$

where $Q_{max} = (mC_p)_{min}\Delta T$ is the maximum deliverable heat transfer, with ΔT being the temperature difference of the hot and cold fluid streams entering the heat exchanger. Using the manufacturer's data, at nominal design conditions, a combined effectiveness of 0.5 is used and hence included in the model for both heat exchanger systems. This means that, in practice, both heat exchangers can possibly deliver a final temperature of the gas which is the average of the temperature of gas entering the heat exchanger and that of the ambient air. Eq. (17) can thus be used to obtain a simplified form which gives a direct evaluation of final temperature of the working gas. As an instance, during charge, gas exit temperatures are given by

$$T_{3a} = \frac{T_3 + T_{amb}}{2} \text{ for HX3}$$

$$T_{1a} = \frac{T_1 + T_{amb}}{2} \text{ for HX1} \tag{18}$$

Apart from the losses stated above, gas transferring ducts can also incur some losses (thermal and gas turbulence) which have been ignored in the model as these are expected to be very small.

4. Experimental results of the demonstrator

As aforementioned, during ongoing testing the demonstrator was operated at part-load as one of the cylinder valves in the heat pump/ engine did not function well at high design pressures when it was operated at full-load. Hence, the tests were conducted at part-load to examine the thermodynamical aspects of compression and expansion processes of the novel heat pump/engine. The RTE at full-load was then evaluated numerically using the performance tested through these

experiments.

4.1. Thermal stores

The nominal charge/discharge duration of the stores is 4.0 hrs at full-load. Although the heat pump/engine was operated for sufficient length of time to establish equilibrium conditions and adjust correct valve timings of the heat pump/engine, the thermal stores were not charged completely. Therefore, no pressure and temperature data was captured from either store in the present experimental work. The thermal stores were then tested separately to demonstrate and validate the concept of layered thermal storage and assess its effectiveness for use in a PHES system (not included in present paper).

4.2. Heat pump/engine

In the first step towards assessing the heat pump/engine performance and evaluating the system RTE, the demonstrator was run at $N = 250$ rpm, with nitrogen as working gas. The HS pressure was varied between ~3–5 bar whereas the CS pressure was maintained at nearly ambient conditions. With pressure ratio, β, being the variable parameter, 12 datasets were obtained from the demonstrator runs. The working speed was kept same for all runs. Table 7 states these experimental conditions. Although argon is preferred due to its higher adiabatic index, the following tests were conducted using nitrogen which yields relatively similar thermodynamic performance, as will be shown shortly in Section 5.1.

The experimental P-V plots obtained from the heat pump/engine during a charge cycle are shown in Figs. 10 and 11. (These plots belong to the dataset obtained at $\beta = 3.25$). Fig. 10 shows a P-V plot (left) together with P-θ plot (right) for one of the upper cylinders undergoing compression. The plots were captured using LabVIEW control software which reads and publishes all the sensor data to a dedicated GUI. It is notable that the measurement data was collected when the demonstrator reached a steady state operation. Pressure was directly measured from the Kulite sensor whereas volume was calculated using data from linear magnetic encoder and cylinder geometry. A total of 6000 measurements were recorded for one cycle. Fig. 11 shows redrawn plots for all three cylinders. Each plot is drawn by averaging data for 10 consecutive engine revolutions to smooth out any cycle-to-cycle variations which may have occurred due to signal noise in the measured data. HC1 and HC2 are named to identify upper and lower double-acting hot cylinders undergoing a compression cycle whereas CC corresponds to bottom single-acting cold cylinder undergoing an expansion cycle (refer to Fig. 5 for cylinders layout). As can be seen in Fig. 11, the suction and discharge curves have a wavy pattern in case of both compression cylinders. This is due to the acoustic noise picked by the sensors. During calibration of the Kulite sensors it was revealed that the sensitivity of sensors was not stable under given range of pressures and temperatures. It was found that high temperature expected in the upper cylinders (HC1 and HC2) was the primary cause of drift in sensitivity. To mitigate this problem the sensors were placed on tubes extending from cylinder head

Table 7
Experimental conditions and summary of results.

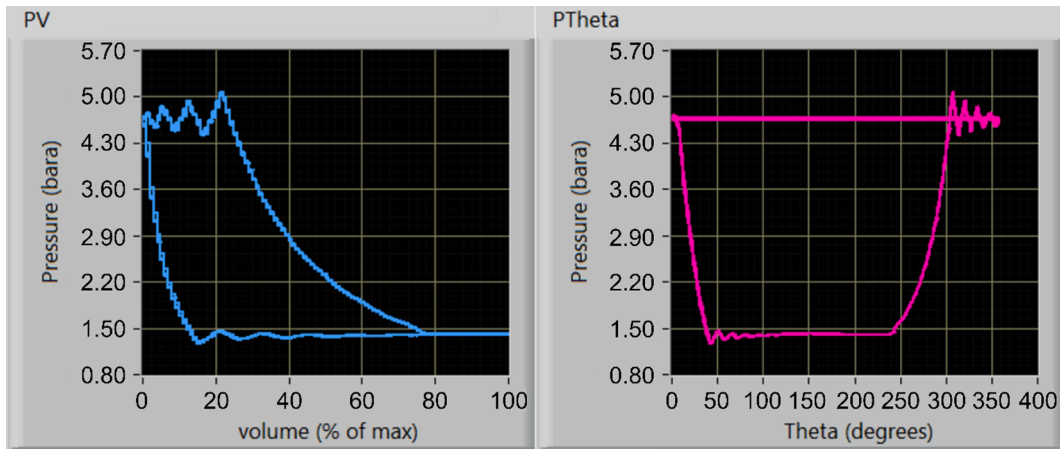|	This study	Howes [43]
Working gas	Nitrogen	Air
Operating speed, N [rpm]	250	318
Intake pressure, P_{4-1} [bar]	~1.0–1.38	1.0
Discharge pressure, P_{2-3} [bar]	~3.0–5.0	1.6
Pressure ratio, β [–]	2.9–4.57	1.6
Polytropic index, n [–]	1.22–1.28 (measured)	Not given
Total loss factor, α_{total} [%]	24.97–37.0 (measured)	17.5
Heat loss factor, α_h [%]	18.37 (predicted via Howes model)	17.5
Flow loss factor, α_f [%]	6.6–18.6	0

Fig. 10. GUI screen showing observations for a compression cylinder using nitrogen as working gas at $N = 250$ rpm and $\beta = 3.25$. P-V plot is shown on the left. P-θ plot is shown on the right.
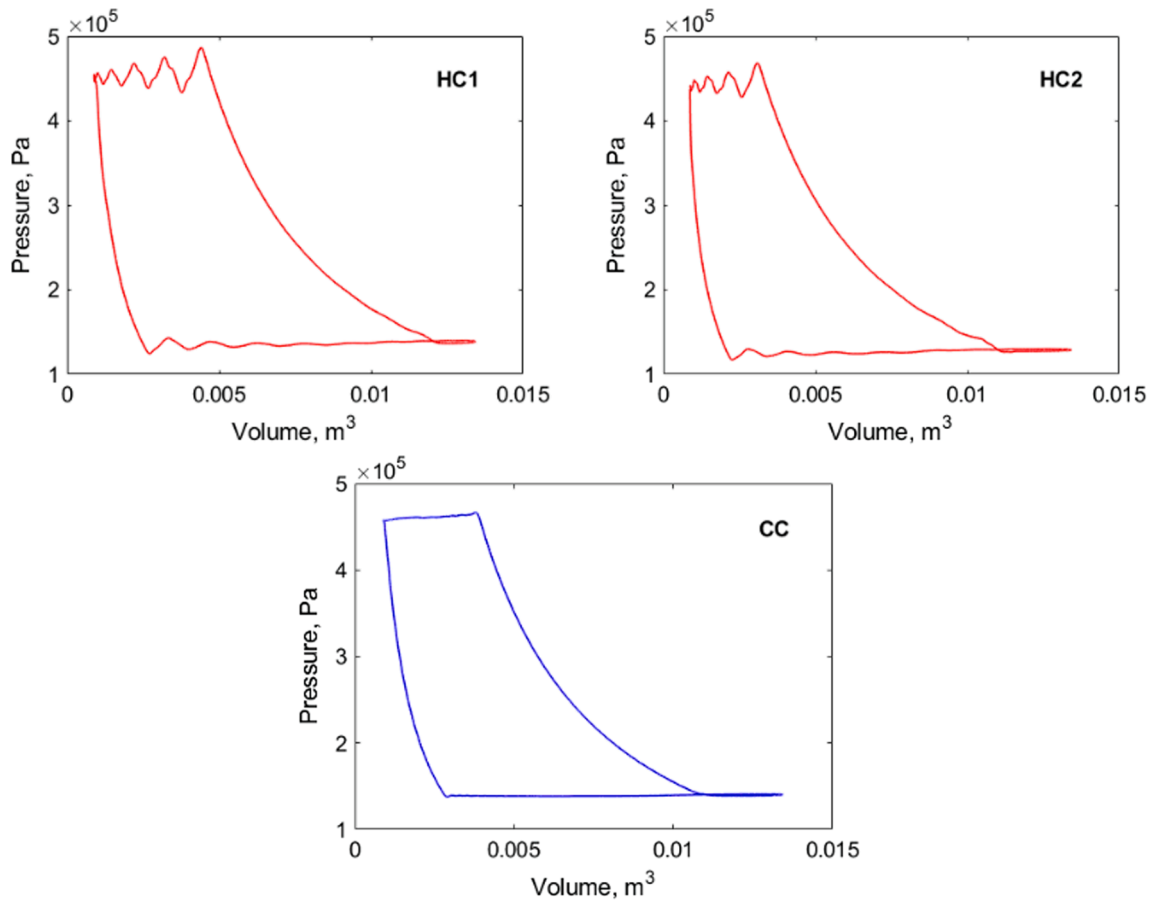

Fig. 11. Redrawn P-V diagrams after postprocessing of experimental data.

valve plate through to external casing so that they remain close to ambient temperature at all times. The acoustic resonance of the tube distorts the frequency response of the sensor which results in wavy pattern. On the contrary, sensor used in the lower cylinder (CC) remains close to ambient temperature, so the sensor is attached directly to the cylinder head valve plate as originally designed, giving a clean P-V plot, as shown in Fig. 11.

4.3. Comparison of experimental compressor P-V cycle with models

The heat pump/engine was designed considering many novel features to achieve compression and expansion processes closely approximating to isentropic cycles. While a true isentropic process is impossible in reality, the degree by which this ideal is approached strongly affects the reversibility of the overall cycle and hence the energy storage RTE. Fig. 12 shows three (overlapping) P-V diagrams for HC1 acting as a compressor. The red solid curve is the actual cycle. The black solid curve is the ideal isentropic cycle whereas dashed curve is the equivalent cycle

predicted using Howes' correlation and scaling method (Appendix A). As can be seen, the measured compression curve deviates from the isentropic curve, 1–2, tending to be inclined towards the side of isothermal curve. To quantify this deviation, various likely losses are to be identified. As mentioned before, besides mass leakage and mixing losses, there are normally two types of losses involved, (1) heat transfer-induced losses, which is subject to finite temperature difference between gas and cylinder walls and (2) valve pressure losses, which are further dependent on velocity and viscosity of the flowing gas and valve geometry. Pressure losses across valves generally occur because of eddying motions and turbulence due to obstruction to gas flow presented by the valves. Whilst the effect of fluid viscosity on the (frictional) pressure drop across pipes and ducts has been extensively studied, the survey of literature reveals that such study is scant as far as flow across valves in reciprocating piston-cylinder devices is concerned. In this study, valve pressure losses were estimated using Eq. (16). The calculated valve pressure losses are very small and even if they are treated within the domain of compression and expansion processes, they will have negligible effect on the process efficiency. As an instance, during charge, the estimated pressure loss at the compressor exit valve is only 42 Pa whilst that at the inlet valve is only 17 Pa, this variation being only due to higher gas density at exit compared to inlet. Similarly, at expander inlet and exit the estimated pressure losses are 79 Pa and 32 Pa respectively. Ignoring valve pressure losses, it is very likely that the compression process deviates from the isentropic curve largely due to parasitic heat loss from gas to cylinder walls. Such in-cylinder heat transfer losses play a dominating role among others, and they have a greater impact on the system RTE, as will be discussed in Section 5.1.

4.3.1. Comparison with Howes' model

Using the correlation presented by Howes and applying scaling method on the current demonstrator, a heat loss factor, α_h, of 18.37 % is predicted corresponding to a polytropic index of 1.31, curve 1–2′ in Fig. 12. As the correlation is independent of β, the predicted value of α_h will be same for all 12 datasets. Note that $\alpha_h = 18.37$ % means that 18.37 % of isentropic work of compression has been lost in the form of heat by the gas to the cylinder walls. In the absence of irreversibilities i.e., in an ideal situation, this percentage of work would actually have been used to further raise the internal energy of the gas which in fact is the requirement for an efficient energy storge cycle. Notwithstanding, as is clear from the figure, the experimental compression curve deviates further from the model curve. The experimental curve was fitted using a curve fitting tool and a polytropic index of 1.25 was obtained ($PV^{1.25} =$
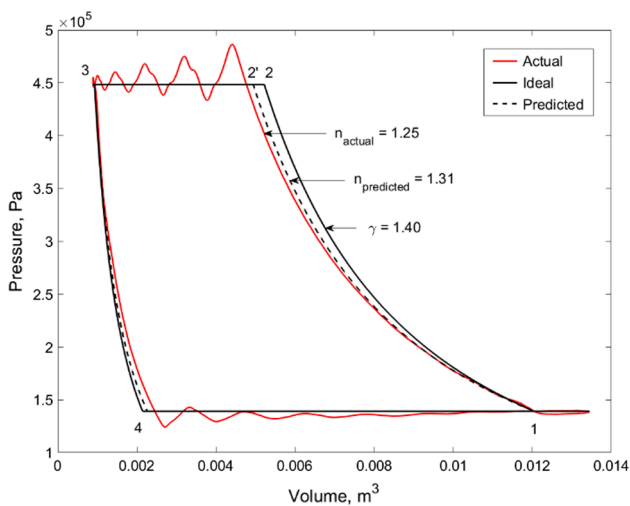
const). This indicates a relative error of 4.6 % in terms of polytropic index. It is yet unclear what is the reason for this excessive loss, however, this may be because of either poor sealing of the valve or the flow past piston rings. It is observable from the P-θ diagram (Fig. 10 (right)) that the plot has sharp corners strongly implying that the valve opening and closing events were precise. Hence, flow leakage may be the reason which can be quantified in a similar way by defining a flow leakage factor, α_f. This in fact is obtained by substituting the measured value of polytropic index, 1.25, in Eq. (12) to calculate the so-called total loss factor of 30.46 %. Subtracting the predicted value of heat loss factor from this total loss factor yields a flow loss factor of about 12 % for the dataset being analysed i.e., at $\beta = 3.25$.

The effect of β on the polytropic index and consequently α_h is also investigated. Fig. 13 displays the values of polytropic index from the 12 runs at different pressure ratios. Table 7 presents the summary of results along with experimental conditions. It can be observed that at relatively lower values of β, the experimentally determined polytropic index is in the close range to that predicted by using Howes' model ($n = 1.31$), with measured index reaching as high as 1.28 in which case α_f is nearly halved to 6.6 % from 12 %. At higher β Howes' model seems to have underpredicted α_h suggesting a higher resulting value of α_f. However, it is also possible that the flow leakage is relatively increased at higher working pressure due to insufficient valve sealing. In addition to this, it should be noted that Howes performed their experiments at a lower pressure ratio: $\beta = 1.6$, and the validity of their correlation is not yet proven at higher pressure ratios. Therefore, there might be some uncertainty associated with identifying this loss, especially at higher pressure ratios, due to adjusted Howes' correlation and, as such, an increased leakage may not be the actual case at any given pressure ratio. Nonetheless, these loss estimates provide a useful insight of the problem in an overall scenario. Flow leaks are highly undesirable for any reciprocating machine operation for all the practical reasons and therefore simulation results of the numerical study presented in Section 4.4 and 5 do not consider this loss.

4.3.2. Comparison with conventional heat loss models

The in-cylinder heat transfer has been further analysed using the quasi-standard models developed for compressors and internal combustion engines. Fig. 14 shows the comparison between experimental results and predicted results from four models in the form of instantaneous gas-wall heat flux, $\dot{q}_w$, plotted against the crank angle, θ, for the same compression cylinder (HC1). The experimental curves are plotted using the P-V measurements and time data from the same typical run as in Figs. 10-12. Instantaneous mean gas temperature in the cylinder and
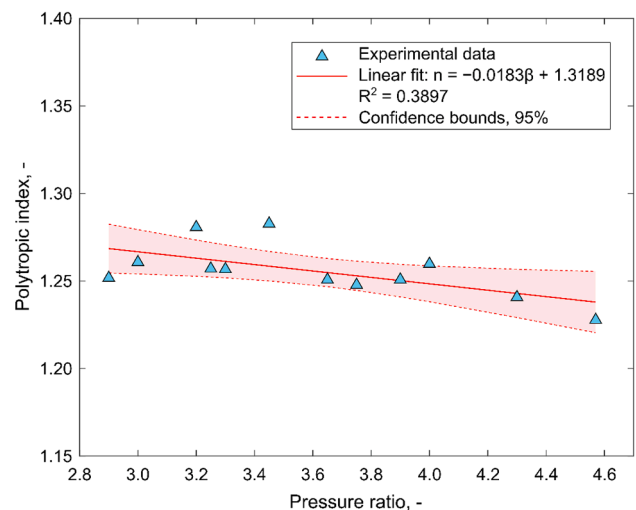

Fig. 12. Comparison of experimental P-V plot of HC1 with reversible adiabtic cycle and Howes' model plots. 1–2: compression, 2–3: discharge, 3–4: reexpansion and 4–1: suction.

Fig. 13. Effect of β on polytropic index for compression curves. Data is fitted using the linear regression model.

internal energy were computed directly using the ideal gas equation of state, $PV = mRT$, for a polytropic compression process. Work was computed directly from the P-V plot using trapezoidal rule. Finally, the wall heat transfer rate was computed from the knowledge of internal energy and work using 1st Law of thermodynamics as follows

$$\dot{Q}_w = m_g c_v \frac{dT}{dt} + P \frac{dV}{dt} \qquad (19)$$

As the heat pump/engine was not equipped with surface thermocouples, no surface heat transfer measurements were possible. Kornhauser [63] argued that surface temperature measurements are useful in case of a fired internal combustion engine as such local measurements may not be representative of heat transfer for the entire cylinder. Comparison of experimental and model plots shows that $\dot{q}_w$ is negative during compression and positive during re-expansion indicating a heat loss by the gas to the wall during compression and heat gain by the gas from the wall during re-expansion. A note should be made here that the models developed for gas springs (Kornhauser and Lekic) do not involve suction and discharge strokes as opposed to those developed for 4-stroke internal combustion engines (Annand and Lawton). In the present work, only heat transfer for compression and re-expansion processes has been calculated and shown in the figure. Since part of the compression and re-expansion strokes is consumed in the discharge and suction of the fresh working gas in one complete revolution, it would make no sense to model these isothermal processes. Furthermore, the models developed for engines are applied on current situation with the same value of pressure ratio: $\beta = 3.25$, and therefore the compression and re-expansion strokes end according to the valve timing as is the case in the present experimental situation.

All models underpredict the wall heat flux which ranges from -8.6×10^4 W/m^2 to $+3.2 \times 10^4$ W/m^2 for the measured data. Kornhauser and Lekic models yield a peak heat flux of -4.9×10^4 and 5.2×10^4 kW/m^2, respectively, with no positive heat flux (wall-to-gas). Annand model yields a heat flux ranging between -3.9×10^4 and $+3.0 \times 10^4$ W/m^2. Lawton model yields a heat flux from -6.6×10^4 to 8.4×10^4 W/m^2. It is observed that the models developed for gas springs tend to significantly deviate from those developed for conventional combustion engines as well as current heat pump/engine involved in this study. The model presented by Lawton agrees well with the measured data particularly for the compression process. For re-expansion process, the model underestimates the wall-to-gas heat transfer. Difference between model
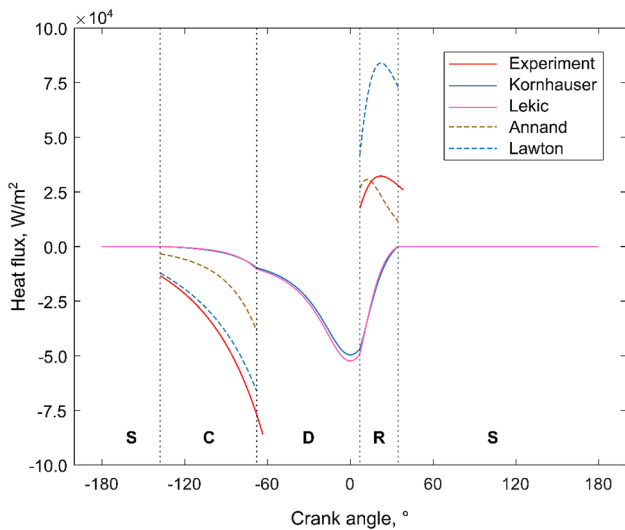
results is primarily because of different experimental conditions and several factors coming into play for governing the underlying heat transfer mechanism, such as piston-cylinder geometry, operating speed, and other working conditions. For gas springs peak heat flux occurs near the top dead centre. However, for engines and current work, peak heat flux occurs at the end of compression right before the start of discharge stroke. Of importance to note here is that the piston-cylinder machines inevitably involve parasitic gas-to-wall heat loss from cycle to cycle affecting the efficiency which is a well-established phenomenon. As the current system was operated at low speed, the heat loss is significant. However, at higher speeds the compression process tends to become adiabatic which is a well-known fact and so the process is less likely to generate a heat loss which is in excess of acceptable limits.

The influence of β on $\dot{q}_w$ is also discussed. A comparison is drawn in Fig. 15 between the measured and predicted values of heat loss, Q, during the compression process using Lawton model for the 12 datasets. The parity plot reveals that at lower β the measured heat loss matches with that predicted using the model. On the contrary, at higher β, the model underestimates the heat loss implying that the increasing deviation observed in the experimentally determined values at increasing β may be associated with a respective increase in mass leakage; this is the same trend as was observed using Howes' model in the previous section.

4.4. Estimation of demonstrator's overall performance at part-load

The nominal electrical design power of the demonstrator is ~150 kW$_e$. Considering the mechanical losses and electrical losses caused by the motor-generator (MG) system, the thermodynamic design power received by the heat pump/engine for charging of thermal stores is reduced to ~132 kW$_t$. This is actually the maximum power that is required for the demonstrator to operate at full-load conditions using ideal (reversible adiabatic) reciprocating heat pump/engine. With this, in the absence of any losses in the thermal stores, the maximum discharge power will be ~117 kW$_e$. In practice, the heat pump/engine has a polytropic efficiency of 98 % and nominal heat loss factor of 2 %; both factors offset each other to result in a so-called isentropic compression/expansion process (see Eq. (12)). There is very little published data on polytropic efficiency, and so its value was fixed at 98 % in accordance with previous theoretical studies. On the other hand, heat loss factor which has been extensively discussed in Section 4.3 is subject to variation depending upon characteristics of the compressor/expander machine and operating parameters. Any increase in heat loss factor, together with thermal store losses, will subject the system maximum thermodynamic and consequently the electrical power to reduce, as will be demonstrated numerically in the next section. During current
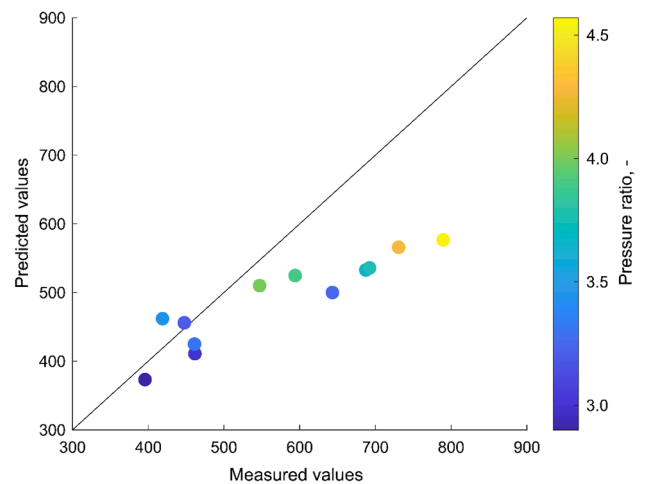
Fig. 14. Comparison of $\dot{q}_w$ versus θ for one revolution of the heat pump/engine starting from the bottom dead centre. Solid curves represent the two gas-spring models whereas dashed curves represent the two internal combustion engine models. S: suction, C: compression, D: discharge and R: re-expansion.

Fig. 15. Effect of β on measured and predicted compression heat loss determined in Joules.

experimental work, at $\beta = 3.25$, the system was run at much lower power, 7.09 kW$_t$, in the charge mode (in comparison to the nominal design power of ~132 kW$_t$). According to simulation results, ignoring the mechanical and electrical losses, one-off charge–discharge cycle produces a thermodynamic RTE of 76.70 %. Including these losses,[3] the electricity-to-electricity RTE turns out to be 57.26 %.

Mass flow rate, $\dot{m}_g$, was calculated by applying the ideal gas law, $PV = mRT$, using measured P-V data which, in this case, is 0.1 kg.s^{-1} in comparison to the design value of 1.26 kg.s^{-1}, this being due to lower pump/engine speed together with lower values of β and τ. Overall effect is that the system consumes very little power and consequently because of decreased mass flow rate, the thermal stores charge and discharge in significantly longer periods, 38.0 hr and 34.9 hr respectively. System storage capacity becomes 269.72 kWh$_t$ during charge and 206.88 kWh$_t$ during discharge.

5. Simulation results of different case studies and performance at full-load

As part of a comparative study to examine how the PHES demonstrator would perform under different conditions, eight different cases were simulated and analysed here. Cases differ based on i) working fluid, ii) pump/engine speed, *N*, and iii) pressure ratio, β, as presented in Tables 8 and 9. There are two sets of chosen values for each variable parameter. The aim of the numerical analysis presented here is to predict the performance at full-load conditions. It is known that any variation in the performance of thermal stores is strictly tied to the given boundary conditions i.e., $\dot{m}_g$ and relevant thermodynamic properties, these being dictated by the pump/engine action. Although each case considers the actual, experimental performance of the pump/engine presented in Section 4, the cases have been further investigated considering exemplary isentropic compression and expansion processes ($\eta = 98$ % and $\alpha_h = 2$ %). The collected experimental P-V data from the demonstrator run at $\beta = 3.25$ belongs to case (1). Cases (1) to (7) correspond to operation at multiple part-load conditions whilst case (8) represents nominal design (full-load) conditions. It should be noted that each case deals with the pressures and temperatures which are well within the range of practical limits of the construction materials used for the thermal stores, pump/engine and ducting.

Unless otherwise stated, datum temperatures are set at pre-defined values for each case: HP datum is set at 35 °C which is the required temperature of the gas entering the E/HS during charge/discharge; whereas LP datum is set at 170.82 °C which is the required temperature of the gas entering C/CS during charge/discharge. A comparatively higher value of LP datum temperature is considered here because of higher CS working pressure of 3 bar at nominal design conditions (case 8); this allows to achieve a target HS temperature and pressure of 773.15 K and of 12 bar respectively with argon as working gas. Respective charging temperatures, T_c, at the stores' ingress are obtained by using Eq. (12) and are shown in the tables showing results summary. Furthermore, HS and CS are assumed to be at respective datum temperatures before first charge.

5.1. Discussion of simulation results

Tables 8 and 9 present the summary of simulated results for each case. As expected, few (very general) trends can be observed. Whilst the focus is on the RTE$_t$, system power (in kW$_t$), storage capacity (in kWh$_t$) and charge/discharge durations (in hr) have also been analysed here. It should be noted that the RTE$_t$ will not simply be a ratio of the system

powers during discharge and charge, rather it will be the ratio of the total amount of works integrated over the whole discharge and charge cycles, or alternatively the ratio of respective storage capacities manifested by thermal stores.

Notably, in contrast to some of the published works, the power during any phase of the present storage process remains nearly constant. This is due to characteristic feature of the demonstrator stores – layering – which is due to that narrow thermocline allows nearly constant gas outlet temperature from the storage and thus uniform power output from the engine. A robust control system together with a flywheel connected to the crankshaft always act to minimise any sharp instantaneous power fluctuations which may occur due to movement of thermal front between successive layers, thereby ensuring a fairly smooth operation in compliance with grid demand. According to results presented in [42], the RTE of a PHES system (having a non-layered store) can be really poor (6.34 %) which is due to early stopping of the discharge cycle as a result of output power dropping below certain fraction of its starting value. Another study [45] highlighted this issue where the discharge power is shown to decline continuously due to thermal energy reduction in the stores. As stated before, current system overcomes this drawback by using layered thermal stores. As an instance, variation of instantaneous power for the first charge–discharge cycle is shown in Fig. 16 for case (8) i.e., with argon at full-load. There are two datasets plotted on the figure which correspond to the actual and isentropic cases. As can be seen in the figure, for both actual and isentropic cases, the input power is nearly uniform during charge with some momentarily sharp variations (indicated by spikes) taking place due to shifting of the progressing front to the new layers in the stores. During discharge, the output power, which is slightly reduced compared to the input power during charge, shows rather rounded variations for both cases. The rather fine pattern of the power during charge is due to initial uniform temperature of the stores which is no longer uniform at the start of discharge.

A comparison of power and the RTE$_t$ for nitrogen and argon at two given speeds and pressure ratios is shown in Fig. 17. The figure shows that for any case the discharge power is always lower than the charge power (Fig. 16 also indicates this), this being due to the incurred losses at various points around the cycle resulting in slightly decreased pressure ratio during discharge.

Both nitrogen and argon yield efficiencies falling within a narrow range at respective β and *N*, with maximum observed variation of merely 2.7 %. As can be seen on the figure, for a particular speed, at a higher value of β, the RTE$_t$ is slightly lower than at a lower value. However, this behaviour is relatively pronounced for corresponding isentropic cases (see Tables 8 and 9 for this comparison). This situation also results in reduced charge and discharge durations which is mainly due to the increased mass flow rate yielding higher rate of heat transfer. Similarly, for any pressure ratio, at a higher speed, the RTE$_t$ is slightly lower compared to that at a lower speed. However, this penalty in the RTE$_t$ is offset by significantly reduced charge and discharge durations, this is again evidentlydue to a direct increase in mass flow rate (and hence the resulting heat transfer) at a higher speed. Irrespective of operating speed and β, for any case, an improvement in the RTE$_t$ can be noticed when the pump/engine behaves isentropically, however, general trends mentioned above remain the same. This improvement is relatively significant at lower β, e.g., for nitrogen, at 1000 rpm, 8.9 % improvement is observed for case (2) compared to a 5.8 % increase for case (4). Charge and discharge durations (which are largely dependent on mass flow rate) do not change much. Similarly, for argon at 1000 rpm, 6.9 % increase is observed at lower β of case (6) in comparison with 5.7 % increase at higher β of case (8).

Fig. 17 also highlights that lower β and speed result in slightly improved RTE$_t$, but it comes at the expense of sufficiently decreased power and capacity. Clearly a choice will have to be made in achieving the required RTE$_t$ at the desired power and capacity, which obviously will be inclined towards attaining more power and capacity for a given

---

[3] In a complete energy storage cycle, the PHES system undergoes energy conversions four times: twice in charge, and twice in discharge. An electricity-to-electricity RTE can be calculated against any quoted thermodynamic RTE by using mechanical and electrical efficiencies of 90% and 96% respectively.

Table 8
Results summary with nitrogen as working fluid.

Case	Pressure ratio β		Charge temperature T_c, [K] HS	CS	Speed N, [rpm]		Time t, [hr]	Power P, [kW$_t$]	Energy capacity [kWh$_t$]	Thermodynamic Round-trip efficiency RTE$_t$, [%]	Electricity-to-electricity Round-trip efficiency RTE$_e$, [%]
1	4.48/ 1.38	Actual	586.5	235.8	250	C	38.0	7.1	269.7	76.7	57.3
						D	34.9	5.9	206.9		
		Isentropic	620.2	220.6		C	35.6	9.6	340.3	85.7	64.0
						D	32.0	9.1	291.6		
2		Actual	614.7	225.4	1000	C	9.1	37.3	341.0	74.9	55.9
						D	8.2	30.9	255.4		
		Isentropic	620.2	220.6		C	9.0	38.2	343.1	83.8	62.6
						D	8.0	35.7	287.5		
3	12.0/ 1.72	Actual	696.8	199.9	250	C	30.8	18.1	555.8	76.2	56.9
						D	26.9	15.7	423.6		
		Isentropic	773.0	177.0		C	31.1	24.5	760.6	80.8	60.3
						D	26.0	23.6	614.6		
4		Actual	759.6	184.0	1000	C	7.8	94.8	740.4	73.9	55.2
						D	6.6	82.6	547.5		
		Isentropic	773.0	177.0		C	7.8	97.7	764.7	79.7	59.5
						D	6.6	93.0	609.7		

C: charge; D: discharge. For cases (3) and (4), CS pressure is slightly increased to 1.72 bar to achieve a target HS temperature of 773 K. For actual cases (non-isentropic), polytropic index is 1.31 at 250 rpm and 1.38 at 1000 rpm.

Table 9
Results summary with argon as working fluid.

Case	Pressure ratio β		Charge temperature T_c, [K] HS	CS	Speed N, [rpm]		Time t, [hr]	Power P, [kW$_t$]	Energy capacity [kWh$_t$]	Thermodynamic Round-trip efficiency RTE$_t$, [%]	Electricity-to-electricity Round-trip efficiency RTE$_e$, [%]
5	4.48/ 1.38	Actual	629.4	220.4	250	C	49.4	7.6	375.4	76.7	57.3
						D	44.5	6.5	287.9		
		Isentropic	708.9	193.0		C	49.3	11.7	575.6	83.0	62.0
						D	42.6	11.2	477.9		
6		Actual	693.1	200.9	1000	C	12.4	44.3	547.8	74.8	55.8
						D	10.8	37.9	409.5		
		Isentropic	708.9	193.0		C	12.4	46.7	578.0	81.7	61.0
						D	10.7	44.1	471.9		
7	12.0/ 3.0	Actual	667.2	208.4	250	C	23.0	20.7	476.0	75.8	56.6
						D	20.4	17.7	360.8		
		Isentropic	773.0	177.0		C	23.3	32.8	762.0	80.4	60.0
						D	19.5	31.4	612.8		
8		Actual	751.4	186.0	1000	C	5.8	122.8	716.4	73.1	54.6
						D	4.9	105.9	523.6		
		Isentropic	773.0	177.0		C	5.8	130.8	764.8	78.8	58.8
						D	4.9	123.6	602.7		

C: charge; D: discharge. Polytropic index is 1.42 at 250 rpm and 1.61 at 1000 rpm.

PHES system.

Comparison of the two working gases indicates that for the given installation size of the demonstrator, at design conditions, nitrogen offers almost equal storage capacity and RTE$_t$ but at the expense of lower power and greater cycle durations compared to argon (referring to cases (4) and (8) here). This implies that argon is a preferred working gas for the system. In the present scenario, since the size of the pump/engine is fixed, and we can only vary operating conditions within a practical range, it is in fact the storage system size and capacity will play its role in determining suitability of a working gas. To better understand we will analyse results considering storage system size, capacity and cycle time simultaneously keeping in mind that a thermodynamically attractive system is no longer feasible, by any chance, where higher capacity is achieved at the cost of prolonged charge/discharge durations.

Within limitations imposed by the material constraints, the system size and capacity are clearly favoured by higher pressure ratio, β, (and hence the resulting temperature ratio, τ) and operating speed, N. Fig. 18 is plotted for both working gases at higher β to indicate how system size increases linearly with the operating speed. Here noteworthy point is that greater speeds favour close to isentropic compression (and

expansion) with reduced heat loss (and gain) which is the regime of interest for PHES applications.

The effect of heat pump/engine heat loss/gain due to irreversible in-cylinder heat transfer on system RTE$_t$ has also been studied. The results are shown in Fig. 19. It should be noted that to study this aspect of the demonstrator, simulations were run by using nine different values of α_h predicted directly via Howes' correlation. For this purpose, the operating speed (taken as the independent variable) was varied between 200 and 1000 rpm to approximately represent the practical range of speeds at which the demonstrator can be operated. Since N inversely relates with α_h (Fig. 8), it is convenient to use N as the independent variable for determining α_h and rest of the simulation conditions. Nine datasets were thereby obtained as marked on the figure. Interestingly, the results reveal that as the compression heat loss (or expansion heat gain) factor decreases, the RTE$_t$ also decreases. However, this decrease in RTE is marginal; 3.13 % drop is observed with a 28 % decrease in α_h when N is increased from 200 to 1000 rpm. In any case, this does not imply that a higher heat loss factor should be allowed to produce higher efficiency. Due to several factors intricately linked this trend cannot be easily explained. Largely, the reason lies in the fact that at low speeds the mass
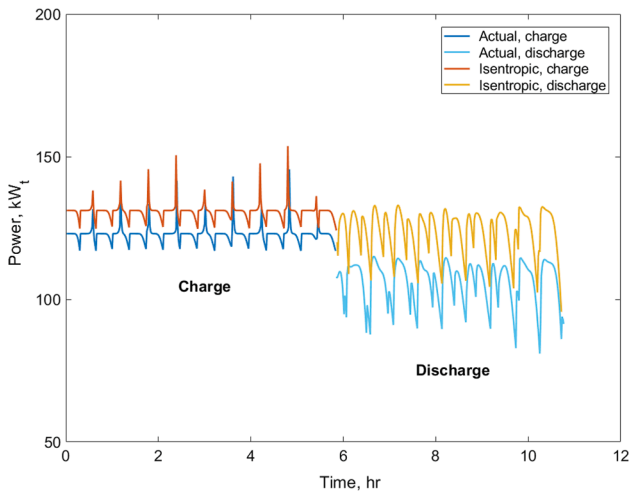
Fig. 16. Thermodynamic power variation during one storage cycle using argon at $N = 1000$ rpm and $\beta = 4.0$ (case (8)). The dataset with higher input/output power refers to pseudo-ideal heat pump/engine cycle whereas that with lower power input/output refers to actual heat pump/engine cycle incurring a certain heat loss.
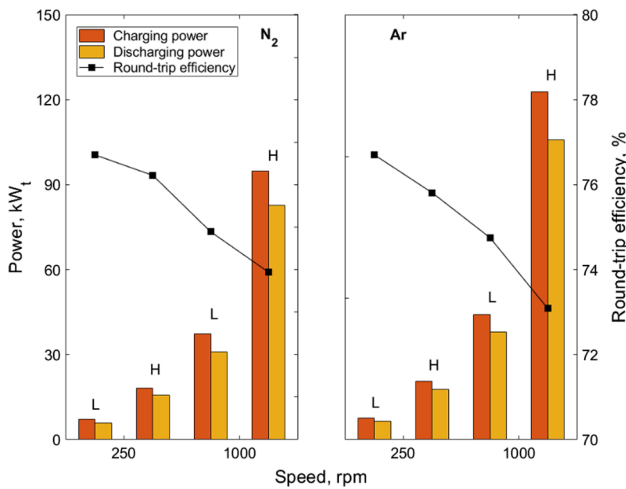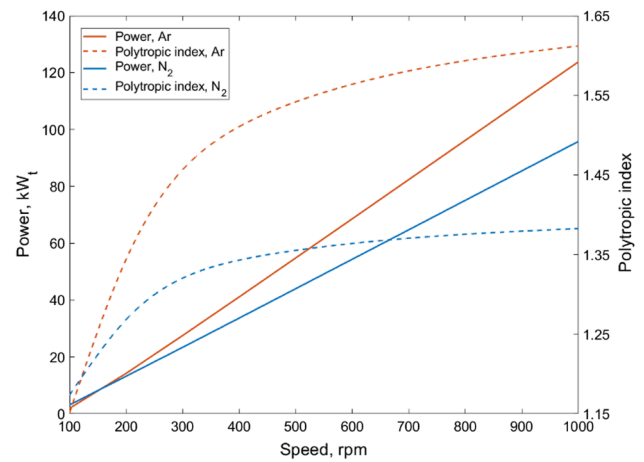

Fig. 17. Thermodynamic power and RTE$_t$ variation in different cases. Respective isentropic cases are not shown. L and H corresponds to low- and high-pressure ratio respectively.

flow rate is decreased in addition to generating high heat pump/engine heat losses. This, in turn, has a direct effect on the system charge and discharge powers and respective times required to charge and discharge the thermal stores. The bottom part of Fig. 19 shows these trends; with a decrease in α_h the charge and discharge powers are increased whereas respective cycle times are decreased. The combined effect is that a minor reduction in RTE$_t$ is observed. It can be asserted that higher pump/engine heat losses are not favourable to achieve slightly increased RTE$_t$ as it is not practicable due to much reduced system powers and increased cycle times.

5.2. Cyclic operation

The results presented above relate to single or one-off charge–discharge operation. Practically, a storage system might need to undergo multiple charge and discharge cycles. Therefore, to evaluate the demonstrator's performance under a cyclic operation, cases (4) and (8) with experimentally observed performance of the pump/engine are considered here. The stores modelling scheme remains the same and the

Fig. 18. System thermodynamic power and polytropic index (evaluated using Howes' correlation) as a function of operating speed.
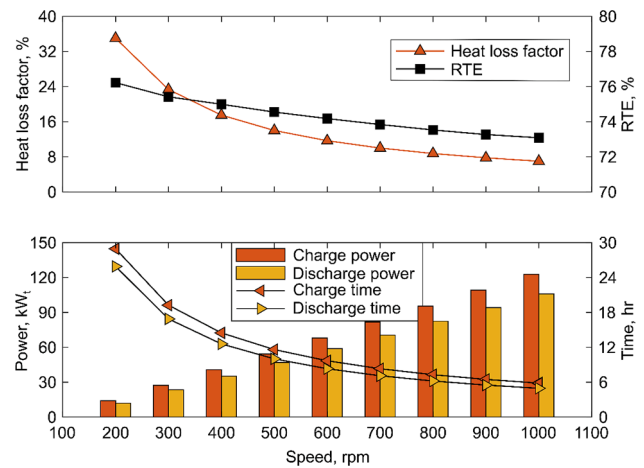
Fig. 19. Effect of compression heat loss (and expander heat gain) factor on powers, cycle durations and resulting RTE$_t$ for argon.

gas flow is allowed to reverse between successive charge and discharge cycles alternatively. The simulations are carried out such that the conditions at the end of any discharge serve as the initial conditions for the following charge. Although practical applications may require the energy to be stored for a certain length of time, however, for simplicity, it is assumed that there is no time gap between any two cycles. Hereby the need for modelling non-operational periods, where conductive losses and thermal leakage may play significant role, is eliminated.

In Fig. 20, results from a cyclic operation are shown for nitrogen and argon for the first 8 cycles. Examination of the results shows that the general comparison between nitrogen and argon presented in the previous section follows the same pattern even in the cyclic operation, as is evident from the figure. Therefore, focusing on the cyclic operation, the results only with argon as the working gas are discussed below.

The system charges in 5.84 hr, discharges in 4.94 hr and yields a RTE$_t$ of 73.09 % in the first cycle. Next cycle shows a marked improvement in the performance as the RTE$_t$ rises sharply to 86.53 % with charge and discharge durations of 4.97 and 5.02 hr respectively. This occurs with a reduction in charge capacity from 716.40 kWh$_t$ of the first cycle to 601.33 kWh$_t$ of the second cycle. Discharge capacity decreases slightly from 523.59 kWh$_t$ to 520.36 kWh$_t$ for these first two cycles. Over the next six cycles, the system performance does not vary much and becomes more predictable when it reaches a steady, periodic state with a RTE$_t$ of about 86 % with nearly identical charge and discharge durations of just above 5.0 hr. An overall improvement after the first cycle is
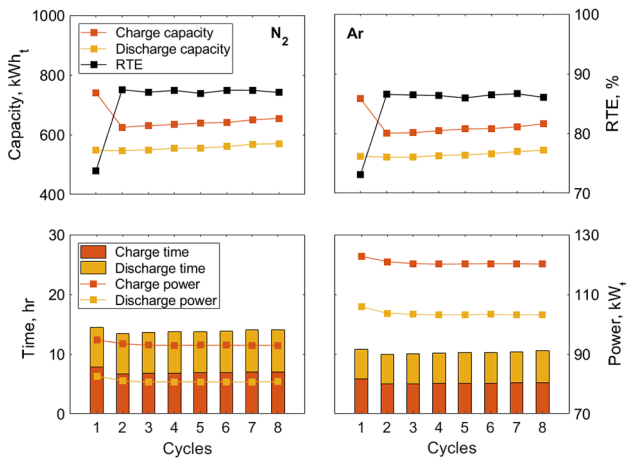
Fig. 20. Cyclic operation of the demonstrator system.

attributed to an even propagation of thermal fronts in the stores becoming more stable as the cyclic operation continues.

A marked improvement in the performance after first cycle is because of the uniform initial conditions at the start of first cycle (similar to a post long-term storage situation when temperature becomes nearly uniform across the stores) employed in the model and the front control strategy specific to layered stores. To better justify this, a store utilisation factor, α_u, can be introduced here. This factor is defined by the ratio of energy exchanged to/from the solid media during a particular cycle to the maximum possible energy which can be stored.

$$\alpha_u = \frac{Q_{stored/released}}{Q_{max}} \qquad (20)$$

where $Q_{max} = m_s c_s(T) \Delta T$. Based on this equation, $\alpha_u = 1$ would correspond to a perfect store. This is practically impossible as it will require sufficiently longer charge durations. The reason is that as the thermal front approaches the end of the store, it becomes wider requiring the charge cycle to be stopped to reduce the increasing workload on the heat exchanger because of excessively rising temperature of the gas exiting the HS (and dropping temperature of the gas exiting the CS).

Fig. 21 shows temperature profiles of HS and CS for the first cycle. As is commonly found in the literature, the charging and discharging temperature patterns of the stores are very well reproduced through simulations. At the beginning of the charge, the thermal fronts are steeper and shorter gradually becoming slanting and wider towards the end. This effect is pronounced for HS. Fig. 21 (a) shows the HS front

which is wider and has not yet passed through full length of the store at the end of charge (trapped between layers 13 and 16). Fig. 21 (c) shows the CS front which is narrower and localised. The CS store is charged up to 10 layers only, this being due to implemented front control strategy which stops the cycle when any one of the stores is charged fully; HS charges first in this case. Temperature-dependent heat capacity of magnetite (obtained using JANAF data [69]) also governs the shape of profiles for respective stores. On first charge, 85.0 % of the HS, and only 63.1 % of the CS are thus utilised. On discharge, CS finishes discharge first which terminates HS discharge as well such that 70.9 % of the HS heat and 53.4 % of the CS cold are recovered. The areas formed by the gradients in the figure are an indicative of these utilisation values.

Variation of solid temperatures for the second cycle is shown in Fig. 22. Here, 70.9 % of HS and 53.7 % of CS are utilised which depicts that nearly same amount of energy which was extracted during first discharge is stored back. On discharge, 71.7 % of the HS heat and 53.8 % of the CS cold are recovered. In fact, an additional amount of energy was required for charging up of early layers of the HS from a completely discharged state which were left uncharged in the next cycle because of an early stop. Furthermore, it is not surprising that cycle 2 yields fractionally higher recoveries compared to cycle 1 as it is very likely that part of the thermal energy stored in the first cycle is reclaimed back over the next cycles due to layered structure. Clearly, cycle 2 yields superior RTE_t (86.53 %) compared to that of cycle 1, this is evidently due to better utilisation (or recovery) of thermal stores after an initial transient phase after which temperature patterns become relatively identical and thermal equilibrium is established.

6. Conclusions

This paper describes the world's first grid-scale Pumped Heat Energy Storage (PHES) system with the aim to demonstrate and evaluate its thermodynamic performance identified by the RTE. This first-of-a-kind demonstration of the PHES technology involved several advanced technical features in its main components – hot and cold thermal stores and reciprocating heat pump/engine device. Whilst the theoretical studies have been performed previously and satisfactory performance has been theoretically proven, the technology clearly lacked validation through experimental data which was the subject of current study. The research work presented in this paper comprised of two main parts: (1) assessment of heat pump/engine performance by conducting experiments and validating it using models, and (2) assessment of overall RTE of the demonstrator by carrying out simulations. Packed-bed type thermal stores employed in the demonstrator offer cost-effective solution and exhibit technically sound thermodynamic performance. A separate experimental study was conducted to demonstrate the novel
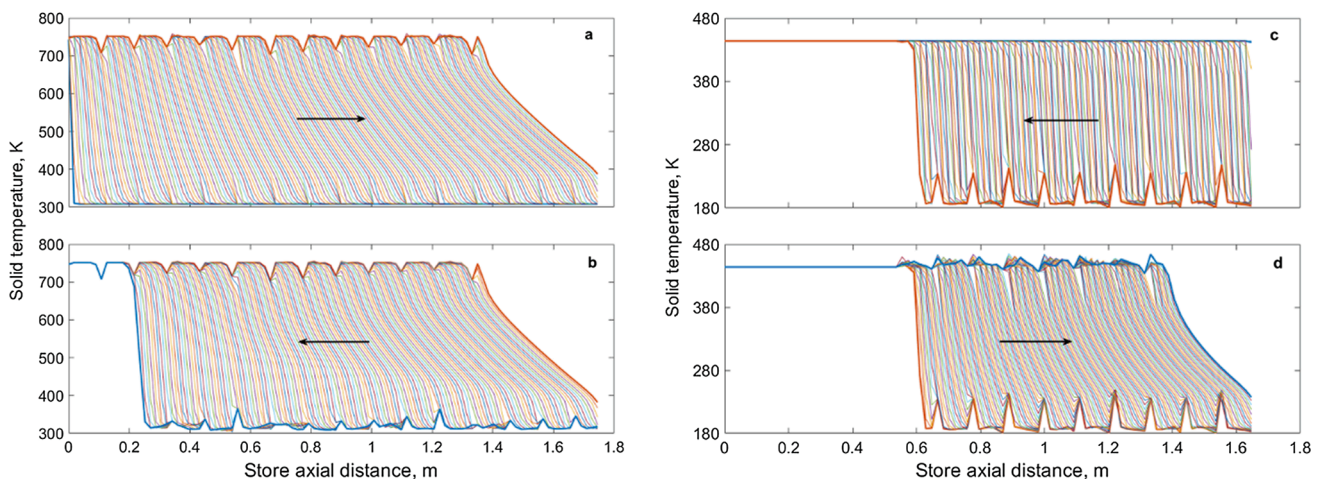

Fig. 21. Temperature profiles of cycle 1. (a) HS charge, (b) HS discharge, (c) CS charge, and (d) CS discharge.
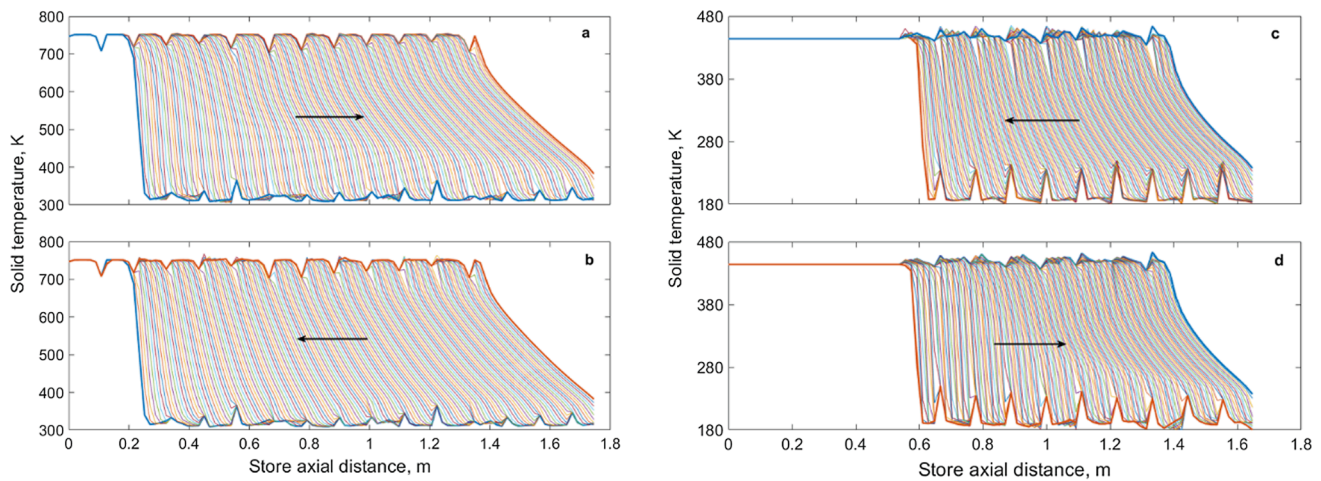
Fig. 22. Temperature profiles of cycle 2. (a) HS charge, (b) HS discharge, (c) CS charge, and (d) CS discharge.

concept of layering applied to these stores. Mathematical model was developed for transient operation of the stores and validated using experiments. The same model has been used in this study to numerically assess the overall RTE of the system in the 2nd part of the study.

For experimental investigation of the heat pump/engine, the demonstrator was operated at part-load, i.e., lower speed and compression pressure ratios using nitrogen. The key P-V data was measured by sensors placed around the heat pump/engine. The recorded data was post-processed to calculate polytropic index. Considering 98 % polytropic efficiency, emphasize was given on determining the undesired heat losses during compression process when the pump/engine operates as a compressor-expander device in the charging mode for energy storage cycle. Observation of experimental data revealed that the polytropic index was not constant and varied in the range: 1.22–1.28, subjected to variation in the pressure ratio in the range: 2.9–4.57, in a way that increasing pressure ratio resulted in slightly lower polytropic index and, therefore, decreased pump/engine performance by some degree. Five models were picked from the literature to critically examine the main factors affecting the polytropic index. Howes model, which gives a straightforward indication of the performance, yielded a heat loss factor of about 18.37 % corresponding to a polytropic index of 1.31. From the other four models, Lawton model agreed with the measured data to the best degree in terms of gas-wall heat flux. Additionally, the experimental data was compared in terms of heat loss at varying pressure ratios using Lawton model. Comparison of these results also showed that with an increase in pressure ratio, the amount of heat lost during compression process is underpredicted. Whilst it is almost impossible to completely reduce such thermal losses even with high level of insulation, the results suggest that the discrepancy is because of gas mass leakage which is pertinent at higher working pressure. Consequently, this may be due to poor valve sealing observed during experiments. Notwithstanding that there is evidence of achieving a higher polytropic index, it is stressed that for PHES technology and other future energy storage systems the use of such bespoke heat pump/engine should not be discouraged only because of unexpected valve functioning at higher pressures.

Using the developed PHES model for simulation purposes, the demonstrator was shown to exhibit a mediocre thermodynamic Round-trip efficiency of 57.26 % at part-load conditions employed during the experimental phase. To evaluate the demonstrator's performance at full-load conditions, simulations were carried out for eight different cases in the second part of the study. Three variables were selected for investigation which were working fluid, pressure ratio and working speed. The first case belonged to part-load experimental conditions whereas the last case belonged to full-load design conditions. The analysis of results showed that best overall performance is obtained at nominal design conditions using argon. At the end the thermodynamic behaviour of the demonstrator under cyclic operation was studied. The main conclusions of the numerical study are as follows:

Although, the system output power and storage capacity can be controlled as per grid demand by varying the pump/engine speed and setting required pressure ratio, from practical point of view it may be highly unfeasible when such system is operated at part-load, this being due to increased charge and discharge durations. An optimisation study can be done in this regard to identify a reasonable range of operating conditions.

Thermal stores can be better utilised, i.e., more storage capacity can be exploited by allowing the thermal front to fully emerge out of the stores, but this will be at the cost of extra work required by the heat exchangers which again will largely depend on the grid demand.

Increase in heat losses in the heat pump/engine may result in slightly higher RTE, however, this is achieved at the expense of significantly reduced system power and increased charge/discharge durations.

In case of a single charge–discharge storage cycle, at full-load conditions and considering the actual heat pump/engine performance observed through experimental work, a thermodynamic RTE of 73.1 % is achieved. When electrical and mechanical losses are also included, a global (electricity-to-electricity) RTE of 54.6 % is realised. On the contrary, in case of the cyclic storage operation at full-load conditions and using the same actual performance of the pump/engine, better energy recoveries from both thermal stores yield about 86 % thermodynamic RTE (and 64.2 % electricity-to-electricity RTE). However, this figure would reach as high as about 95 % if a highly efficient pump/engine is assumed. In this case, when electrical and mechanical losses are also included, about 71 % electricity-to-electricity RTE can be achieved.

Finally, the results of the present study are crucial for analysing the performance of the demonstrator operating at full capacity. By using the design details and manufacturer's data available from a physically developed PHES system, it will be possible to design an up-scaled PHES system along the same lines. The presented results and findings can be used to check the feasibility of any similar real scale project and address possible challenges beforehand.

CRediT authorship contribution statement

Muhammad Tahir Ameen: Software, Formal analysis, Writing – original draft. **Zhiwei Ma:** Conceptualization, Methodology, Writing – review & editing. **Andrew Smallbone:** Conceptualization, Investigation. **Rose Norman:** Conceptualization, Supervision. **Anthony Paul Roskilly:** Conceptualization, Supervision.

Declaration of Competing Interest

The authors declare that they have no known competing financial interests or personal relationships that could have appeared to influence the work reported in this paper.

Data availability

Data will be made available on request.

Appendix A

A scaling is required to a first approximation to use Howes' correlation for analysis of the results from current heat pump/engine of the demonstrator. The scaling parameters involved are: i) cylinder size, ii) working fluid, and iii) running speed [43]. Since both compressor and expander are physically similar in all operational aspects, the most direct assessment of scaling relevant to current reciprocating device is therefore provided by analysis of the compression process only (Fig. 8).

To a first approximation, heat transfer during compression can be represented by

$$\dot{Q}_c = hA\overline{\Delta T} \tag{A1}$$

where $\overline{\Delta T}$ is the average temperature difference between the gas and the cylinder, A is the internal surface area and h is the heat transfer coefficient. The subscript c represents compression process. The Nusselt number related to h is defined by $\mathrm{Nu} = hD/k$.

Assuming heat losses are small, the compression work input is

$$\dot{W}_c \approx \dot{m}_g c_p \Delta T = \rho_g N V_s c_p \Delta T \tag{A2}$$

where V_s is the swept volume and ΔT is the temperature rise through the compressor after compression. The heat loss factor is thus given by

$$\alpha_c = \frac{\dot{Q}_c}{\dot{W}_c} = \frac{(k\mathrm{Nu}/D)A}{\rho_g N V_s c_p} \frac{\overline{\Delta T}}{\Delta T} \tag{A3}$$

V_s scales as D^3 whereas A scales as D^2. Eq. (A3) can therefore be reduced as follows

$$\alpha_c \frac{\mathrm{Nu}}{\mathrm{Re\,Pr}}\left(\frac{\overline{\Delta T}}{\Delta T}\right) \tag{A4}$$

where $\mathrm{Re} = \rho_g N D^2/\mu_g$ is the Reynolds number and $\mathrm{Pr} = \mu_g c_p/k$ is the Prandtl number. Assuming that the Nusselt number and the ratio of temperature differentials, $\overline{\Delta T}/\Delta T$, are the same for the current heat pump/engine as for the Howes' prototype machine, then it follows that

$$\frac{\alpha_{c,d}}{\alpha_{c,p}} = \left(\frac{D_p}{D_d}\right)^2 \times \frac{k_d}{k_p}\frac{c_{p,p}}{c_{p,d}} \times \frac{N_p}{N_d} \tag{A5}$$

where the subscripts d and p correspond to demonstrator and prototype machines, respectively. Using the relationship between running speed and fractional heat loss from Fig. 8 and the cylinder diameter of prototype of 0.3 m, Eq. (A5) can be rewritten as

$$\alpha_{c,d} = \left(\frac{0.3}{0.4}\right)^2 \times \frac{k_d}{k_p}\frac{c_{p,p}}{c_{p,d}} \times \frac{-70.351}{N_d} \tag{A6}$$

Gas properties vary throughout the cycle. However, for the temperature and pressure range concerned, gas properties are almost invariant. Therefore, for simplicity, cycle average values can be used in above equation. Furthermore, as compressor and expander are similar in concept and layout, this parasitic loss will occur twice when charging and twice when discharging. It should be noted that Nusselt number may not be the same for both reciprocating machines and confirmation will only be possible through a detailed experimental analysis under parametric changes. Similarly, the ratio of temperatures may also change as the compressor pressure ratio is changed. Nonetheless, a conservative approximation to a reasonable degree can be reached here based upon initial tests conducted by Howes on the basis of similar geometry.

References

[1] BEIS: Digest of United Kingdom Energy Statistics (DUKES) 2021; 2021.
[2] BEIS: United Kingdom of Great Britain and Northern Ireland's Nationally Determined Contribution; September 2022.
[3] MacKay DJC. Fluctuations and storage. Sustainable Energy without the Hot Air, UIT; 2009.
[4] International Energy Agency. Technology Roadmap: Energy Storage, Paris; March 2014.
[5] U.S. Energy Information Administration, International Energy Statistics database; [accessed 19 October 2022].
[6] EU Energy in Figures, Statistical Pocketbook; 2022.
[7] Shaqsi AZA, Sopian K, Al-Hinai A. Review of energy storage services, applications, limitations, and benefits. Energy Rep 2020;6:288–306.
[8] Chen H, Cong TN, Yang W, Tan C, Li Y, Ding Y. Progress in electrical energy storage system: a critical review. Prog Nat Sci 2009;19:291–312.
[9] Luo X, Wang J, Dooner M, Clarke J. Overview of current development in electrical energy storage technologies and the application potential in power system operation. Appl Energy 2015;137:511–36.
[10] Liang T, Vecchi A, Knobloch K, Sciacovelli A, Engelbrecht K, Li Y, et al. Key components for Carnot Battery: technology review, technical barriers and selection criteria. Renew Sustain Energy Rev 2022;163:112478.
[11] Bazdar E, Sameti M, Nasiri F, Haghighat F. Compressed air energy storage in integrated energy systems: a review. Renew Sustain Energy Rev 2022;167:112701.
[12] Olabi A, Onumaegbu C, Wilberforce T, Ramadan M, Abdelkareem MA, Al-Alami AH. Critical review of energy storage systems. Energy 2021;214:118987.
[13] Frate GF, Ferrari L, Desideri U. Rankine Carnot batteries with the integration of thermal energy sources: a review. Energies 2020;13:4766.
[14] McTigue J. Analysis and optimisation of thermal energy storage. Department of Engineering, University of Cambridge; 2016.
[15] Dumont O, Frate GF, Pillai A, Lecompte S, Lemort V. Carnot battery technology: a state-of-the-art review. J Storage Mater 2020;32:101756.

[16] Malta Inc. Our solution. https://www.maltainc.com/our-solution; [accessed 1 August 2021].

[17] Laughlin RB. Pumped thermal grid storage with heat exchange. J Renew Sustain Energy 2017;9:044103.

[18] Siemens Gamesa Renewable Energy. https://www.siemensgamesa.com/explore/innovations/energy-storage-on-the-rise; [accessed 22 October 2022].

[19] Thess A. Thermodynamic efficiency of pumped heat electricity storage. Phys Rev Lett 2013;111:110602.

[20] Steinmann W-D. Thermo-mechanical concepts for bulk energy storage. Renew Sustain Energy Rev 2017;75:205–19.

[21] White A, Parks G, Markides CN. Thermodynamic analysis of pumped thermal electricity storage. Appl Therm Eng 2013;53:291–8.

[22] McTigue JD, White AJ, Markides CN. Parametric studies and optimisation of pumped thermal electricity storage. Appl Energy 2015;137:800–11.

[23] Benato A, Stoppato A. Pumped thermal electricity storage: a technology overview. Therm Sci Eng Prog 2018;6:301–15.

[24] Smallbone A, Jülch V, Wardle R, Roskilly AP. Levelised Cost of Storage for Pumped Heat Energy Storage in comparison with other energy storage technologies. Energ Conver Manage 2017;152:221–8.

[25] Wang L, Lin X, Chai L, Peng L, Yu D, Chen H. Cyclic transient behavior of the Joule-Brayton based pumped heat electricity storage: Modeling and analysis. Renew Sustain Energy Rev 2019;111:523–34.

[26] Wang L, Lin X, Chai L, Peng L, Yu D, Liu J, et al. Unbalanced mass flow rate of packed bed thermal energy storage and its influence on the Joule-Brayton based Pumped Thermal Electricity Storage. Energ Conver Manage 2019;185:593–602.

[27] Zhang H, Wang L, Lin X, Chen H. Technical and economic analysis of Brayton-cycle-based pumped thermal electricity storage systems with direct and indirect thermal energy storage. Energy 2022;239:121966.

[28] Koen A, Farres-Antunez P, Macnaghten J, White A. A low-temperature glide cycle for pumped thermal energy storage. J Storage Mater 2021;42:103038.

[29] McTigue JD, Farres-Antunez P, Markides CN, White AJ. Techno-economic analysis of recuperated Joule-Brayton pumped thermal energy storage. Energ Conver Manage 2022;252:115016.

[30] Zhao Y, Liu M, Song J, Wang C, Yan J, Markides CN. Advanced exergy analysis of a Joule-Brayton pumped thermal electricity storage system with liquid-phase storage. Energ Conver Manage 2021;231:113867.

[31] Koen A, Antunez PF, White A. A study of working fluids for transcritical pumped thermal energy storage cycles. In: 2019 Offshore energy and storage summit (OSES). IEEE; 2019. p. 1–7.

[32] Steinmann W-D, Bauer D, Jockenhöfer H, Johnson M. Pumped thermal energy storage (PTES) as smart sector-coupling technology for heat and electricity. Energy 2019;183:185–90.

[33] Frate GF, Ferrari L, Desideri U. Multi-criteria investigation of a pumped thermal electricity storage (PTES) system with thermal integration and sensible heat storage. Energ Conver Manage 2020;208:112530.

[34] Zhao Y, Song J, Liu M, Zhao Y, Olympios AV, Sapin P, et al. Thermo-economic assessments of pumped-thermal electricity storage systems employing sensible heat storage materials. Renew Energy 2022;186:431–56.

[35] Anderson R, Bates L, Johnson E, Morris JF. Packed bed thermal energy storage: a simplified experimentally validated model. J Storage Mater 2015;4:14–23.

[36] Al-Azawii MM, Alhamdi SF, Braun S, Hoffmann J-F, Calvet N, Anderson R. Experimental study on packed-bed thermal energy storage using recycled ceramic as filler materials. J Storage Mater 2021;44:103375.

[37] Esence T, Bruch A, Fourmigué J-F, Stutz B. A versatile one-dimensional numerical model for packed-bed heat storage systems. Renew Energy 2019;133:190–204.

[38] Zhao Y, Song J, Zhao C, Zhao Y, Markides CN. Thermodynamic investigation of latent-heat stores for pumped-thermal energy storage. J Storage Mater 2022;55:105802.

[39] Albert M, Ma Z, Bao H, Roskilly AP. Operation and performance of Brayton Pumped Thermal Energy Storage with additional latent storage. Appl Energy 2022;312:118700.

[40] Willich C, Markides CN, White AJ. An investigation of heat transfer losses in reciprocating devices. Appl Therm Eng 2017;111:903–13.

[41] Willich C, White AJ. Heat transfer losses in reciprocating compressors with valve actuation for energy storage applications. J Storage Mater 2017;14:322–8.

[42] Benato A. Performance and cost evaluation of an innovative Pumped Thermal Electricity Storage power system. Energy 2017;138:419–36.

[43] Howes J. Concept and development of a pumped heat electricity storage device. Proc IEEE 2011;100:493–503.

[44] Macnaghten J, Howes JS. Energy storage. WO 2009/044139 A2; 2009.

[45] Ruer J. Installation and methods for storing and recovering electrical energy. WO 2008/148962 A2; 2008.

[46] Desrues T, Ruer J, Marty P, Fourmigué J. A thermal energy storage process for large scale electric applications. Appl Therm Eng 2010;30:425–32.

[47] Howes JS, Macnaghten J, Hunt RG, Bennett RG, Wilson AB. Improved thermal energy storage apparatus. WO 2013/160650 A2; 2013.

[48] White AJ, McTigue JD, Markides CN. Analysis and optimisation of packed-bed thermal reservoirs for electricity storage applications. Proc Inst Mech Eng, Part A: J Power Energy 2016;230:739–54.

[49] Lemmon EW, Huber ML, McLinden MO. NIST standard reference database 23: reference fluid thermodynamic and transport properties-REFPROP, Version 9.1. Gaithersburg: National Institute of Standards and Technology, Standard Reference Data Program; 2013.

[50] Schumann TE. Heat transfer: a liquid flowing through a porous prism. J Franklin Inst 1929;208:405–16.

[51] White AJ. Loss analysis of thermal reservoirs for electrical energy storage schemes. Appl Energy 2011;88:4150–9.

[52] Willmott AJ. Dynamics of regenerative heat transfer: Taylor & Francis; 2002.

[53] White A, McTigue J, Markides C. Wave propagation and thermodynamic losses in packed-bed thermal reservoirs for energy storage. Appl Energy 2014;2014.

[54] Wakao N, Kaguei S, Funazkri T. Effect of fluid dispersion coefficients on particle-to-fluid heat transfer coefficients in packed beds: correlation of Nusselt numbers. Chem Eng Sci 1979;34:325–36.

[55] Carman PC. Fluid flow through granular beds. Trans Inst Chem Eng 1937;15:150–66.

[56] Barbour E, Mignard D, Ding Y, Li Y. Adiabatic compressed air energy storage with packed bed thermal energy storage. Appl Energy 2015;155:804–15.

[57] White AJ. Thermodynamic analysis of the reverse Joule-Brayton cycle heat pump for domestic heating. Appl Energy 2009;86:2443–50.

[58] Moss R, Roskilly A, Nanda S. Reciprocating Joule-cycle engine for domestic CHP systems. Appl Energy 2005;80:169–85.

[59] Woschni G. A universally applicable equation for the instantaneous heat transfer coefficient in the internal combustion engine. SAE Technical paper; 1967.

[60] Annand W, Ma T. Second paper: instantaneous heat transfer rates to the cylinder head surface of a small compression-ignition engine. Proc Inst Mech Eng 1970;185:976–87.

[61] Annand W, Pinfold D. Heat transfer in the cylinder of a motored reciprocating engine. SAE Technical Paper; 1980.

[62] Kornhauser A, Smith J. The effects of heat transfer on gas spring performance. J Energy Res Technol 1993;115:70–5.

[63] Kornhauser A, Smith Jr J. Application of a complex Nusselt number to heat transfer during compression and expansion; 1994.

[64] Lekić U. Fluid flow and heat transfer in a helium gas spring. Laboratory of Thermal Engineering, University of Twente; 2011.

[65] Taleb AI, Barfuß C, Sapin P, White AJ, Fabris D, Markides CN. Simulation of thermally induced thermodynamic losses in reciprocating compressors and expanders: influence of real-gas effects. Appl Therm Eng 2022;217:118738.

[66] Lawton B. Effect of compression and expansion on instantaneous heat transfer in reciprocating internal combustion engines. Proc Inst Mech Eng, Part A: J Power Energy 1987;201:175–86.

[67] Rutczyk B, Szczygieł I. Development of internal heat transfer correlations for the cylinders of reciprocating machines. Energy 2021;230:120795.

[68] Ameen MT, Smallbone A, Roskilly AP, Carpenter E. The development of a screen valve for reciprocating heat pump/engine applications. J Renew Sustain Energy 2020;12:054101.

[69] NIST-JANAF thermochemical tables. https://janaf.nist.gov/; [accessed 1 November 2021].